# The inner structure of ΛCDM haloes – I. A numerical convergence study

C. Power,[1]⋆ J. F. Navarro,[2]† A. Jenkins,[1] C. S. Frenk,[1] S. D. M. White,[3] V. Springel,[3] J. Stadel[4] and T. Quinn[4]

[1]*Department of Physics, University of Durham, South Road, Durham, DH1 3LE*
[2]*Department of Physics and Astronomy, University of Victoria, Victoria, BC, V8P 1A1, Canada*
[3]*Max-Planck Institute for Astrophysics, Garching, Munich, D-85740, Germany*
[4]*Department of Astronomy, University of Washington, Seattle, WA 98195, USA*

**ABSTRACT**

We present a comprehensive set of convergence tests which explore the role of various numerical parameters on the equilibrium structure of a simulated dark matter halo. We report on results obtained with two independent, state-of-the-art, multi-stepping, parallel *N*-body codes: PKDGRAV and GADGET. We find that convergent mass profiles can be obtained for suitable choices of the gravitational softening, time-step, force accuracy, initial redshift, and particle number. For softenings chosen so that particle discreteness effects are negligible, convergence in the circular velocity is obtained at radii where the following conditions are satisfied: (i) the time-step is much shorter than the local orbital time-scale; (ii) accelerations do not exceed a characteristic acceleration imprinted by the gravitational softening; and (iii) enough particles are enclosed so that the collisional relaxation time-scale is longer than the age of the Universe. Convergence also requires sufficiently high initial redshift and accurate force computations. Poor spatial, time, or force resolution leads generally to systems with artificially low central density, but may also result in the formation of artificially dense central cusps. We have explored several adaptive time-stepping choices and we have obtained the best results when individual time-steps are chosen according to the local acceleration and the gravitational softening ($\Delta t_i \propto (\epsilon/a_i)^{1/2}$), although further experimentation may yield better and more efficient criteria. The most stringent requirement for convergence is typically that imposed on the particle number by the collisional relaxation criterion. This implies that, in order to estimate accurate circular velocities at radii where the density contrast may reach $\sim 10^6$, the region must enclose of the order of 3000 particles (or more than a few times $10^6$ within the virial radius). Applying these criteria to a galaxy-sized ΛCDM halo, we find that the spherically averaged density profile becomes progressively shallower from the virial radius inwards, reaching a logarithmic slope shallower than $-1.2$ at the innermost resolved point, $\sim 0.005 r_{200}$, with little evidence for convergence to a power-law behaviour in the inner regions.

**Key words:** gravitation – cosmology: theory – dark matter.

## 1 INTRODUCTION

Over the past few decades, cosmological *N*-body simulations have led to impressive strides in our understanding of structure formation in universes dominated by collisionless dark matter. Such simulations have provided an ideal test-bed for analytical theories of structure formation, and have been used to validate and motivate a variety of theoretical insights into the statistics of hierarchical clus-

tering; see, for example, (Press & Schechter 1974; Bardeen et al. 1986; Bond et al. 1991; Lacey & Cole 1993; Mo & White 1996). In particular, *N*-body simulations have played a pivotal role in providing a clear framework within which the cold dark matter (CDM) cosmogony may be compared with observation, and in establishing CDM as the leading theory of structure formation (Davis et al. 1985).

This work has led to the development of a robust theoretical framework which provides an accurate statistical description of structure growth through gravitational instability seeded by Gaussian primordial density fluctuations. It is now possible to predict with great accuracy, and based only on the initial power

⋆E-mail: Chris.Power@durham.ac.uk
†CIAR Scholar and Alfred P. Sloan Research Fellow.

spectrum of the primordial fluctuations, a number of important statistics that characterize the large-scale structure of the Universe; e.g. the mass function and clustering of dark matter haloes and their evolution with redshift [see, for example, Jing (1998), Sheth & Tormen (1999), and Jenkins et al. (2001)] the non-linear evolution of the dark matter power spectrum and correlation functions [see, for example, Hamilton et al. (1991) and Peacock & Dodds (1996)], as well as the topological properties of the large-scale structure [see, for example, Gott, Weinberg & Melott (1987)].

The impact of such simulation work has been greatest in the non-linear regime, where analytical calculations offer little guidance. Recently, and as a result of the development of efficient algorithms and of the advent of massively parallel computers, it has been possible to apply *N*-body studies to the investigation of structure on small, highly non-linear scales. In these studies we can now probe scales comparable to the luminous radii of individual galaxies, thus enabling direct comparison between theory and observation in regions where luminous dynamical tracers are abundant and easiest to observe. Predicting the structure of dark matter haloes on kpc and sub-kpc scales, where it can be compared directly with observations of galactic dynamics, is one of the premier goals of *N*-body experiments, and there has been steady progress in this area over the past few years.

Building upon the early work of Frenk et al. (1985, 1988), Quinn, Salmon & Zurek (1986), Dubinski & Carlberg (1991) and Crone, Evrard & Richstone (1994), Navarro, Frenk & White (1996, 1997), hereafter NFW, found that, independently of mass and of the value of the cosmological parameters, the density profiles of dark matter haloes formed in various hierarchical clustering cosmogonies were strikingly similar. This 'universal' structure can be characterized by a spherically averaged density profile which differs substantially from the simple power law, $\rho(r) \propto r^{-\beta}$, predicted by early theoretical studies (Gunn & Gott 1972; Fillmore & Goldreich 1984; Hoffman & Shaham 1985; White & Zaritsky 1992). The profile steepens monotonically with radius, with logarithmic slopes shallower than isothermal (i.e. $\beta < 2$) near the centre, but steeper than isothermal ($\beta > 2$) in the outer regions.

NFW proposed a simple formula

$$\frac{\rho(r)}{\rho_{\mathrm{crit}}} = \frac{\delta_{\mathrm{c}}}{(r/r_{\mathrm{s}})(1 + r/r_{\mathrm{s}})^2}, \tag{1}$$

which describes the density profile of any halo with only two parameters, a characteristic density contrast,[1] $\delta_{\mathrm{c}}$, and a scale radius, $r_{\mathrm{s}}$. Defining the mass of a halo as that contained within $r_{200}$, the radius of a sphere of mean density contrast 200, there is a single adjustable parameter that fully describes the mass profile of haloes of given mass: the 'concentration' ratio $c = r_{200}/r_{\mathrm{s}}$.

For the sake of this discussion, the two main points to note from the work of NFW are the following: (i) the density profile in the inner regions of the halo is shallower, and in the outer regions steeper, than isothermal; and (ii) there is no well-defined value for the *central* density of the dark matter, which can in principle climb to arbitrarily large values near the centre.

Conclusion (i) is important, because it is a feature of dark halo models that is required by observations. For example, it implies that the characteristic speeds of dynamical tracers may be lower near the centre than in the main body of the system, as observed in disc

galaxies, where the velocity dispersion of the bulge is lower than indicated by the maximum rotation speed of the surrounding disc, as well as in galaxy clusters, where the velocity dispersion of stars in the central cluster galaxy is lower than that of the cluster as a whole. Conclusion (ii) is also important, as there have been a number of reports in the literature arguing that the shape of the rotation curves of many disc galaxies rules out steeply divergent dark matter density profiles [(Flores & Primack 1994; Moore 1994; de Blok et al. 2001), but see van den Bosch & Swaters (2001)], a result that may signal a genuine crisis for the CDM paradigm on small scales [see, for example, Sellwood & Kosowsky (2001) and Moore (2001)].

These general results of the work by NFW have been confirmed by a number of subsequent studies (Cole & Lacey 1996; Fukushige & Makino 1997; Huss, Jain & Steinmetz 1999; Moore et al. 1998; Jing & Suto 2000), although there is some disagreement about the innermost value of the logarithmic slope. Moore et al. (1998), Ghigna et al. (2000) and Fukushige & Makino (1997, 2001) have argued that density profiles diverge near the centre with logarithmic slopes considerably steeper than the asymptotic value of $\beta = 1$ in NFW's formula. Kravtsov et al. (1998), on the other hand, initially obtained much shallower inner slopes ($\beta \sim 0.7$) in their numerical simulations, but have now revised their conclusions; these authors now argue that CDM haloes have steeply divergent density profiles but, depending on evolutionary details, the slope of a galaxy-sized halo at the innermost resolved radius may vary between $-1.0$ and $-1.5$ (Klypin et al. 2001).

Because steep inner slopes are apparently disfavoured by rotation curve data, it is important to establish this result conclusively; if confirmed, it may offer a way to falsify the CDM paradigm on small scales. Unfortunately, observational constraints are strongest just where theoretical predictions are least trustworthy. For example, the alleged disagreement between observed rotation curves and cuspy dark halo models is most evident for sub-$L_\star$ galaxies on scales of $\sim 1\, h^{-1}$ kpc or less. For typical circular speeds of $\sim 100$ km s$^{-1}$, this corresponds to regions where the density contrast exceeds $\sim 10^6$. Orbital times in these regions are of the order of $10^{-3}$ of the age of the Universe, implying that *N*-body codes must be able to follow particles accurately for several thousand orbits. Few cosmological codes have been tested in a systematic way under such circumstances. Furthermore, the CDM haloes that host typical disc galaxies are thought to extend out to a few hundred kpc, implying that the $\sim$kpc scale probed by observations involves a very small fraction of the mass and volume of the dark halo. As a consequence, these regions are vulnerable to numerical artefacts in *N*-body simulations stemming, for example, from the gravitational softening or the number of particles.

Extreme care is thus needed to separate numerical artefacts from the true predictions of the CDM model. In order to validate or 'rule out' the CDM cosmogony, we must be certain that model predictions on the relevant scales are accurate, robust, and free of systematic numerical uncertainties. Although there have been some recent attempts at unravelling the role of numerical parameters on the structure of simulated dark matter haloes, notably in the work of Moore et al. (1998), Knebe et al. (2000); Klypin et al. (2001) and Ghigna et al. (2000), the conclusions from these works are still preliminary and, in some cases, even contradictory.

To cite an example, Moore et al. (1998) argue that the smallest resolved scales correspond to about half the mean interparticle separation within the virial radius, and conclude that many thousands of particles are needed to resolve the inner density profile of dark matter haloes. Klypin et al. (2001), on the other hand, conclude that mass profiles can always be trusted down to the scale of the

---

[1] We use the term 'density contrast' to denote densities expressed in units of the critical density for closure, $\rho_{\mathrm{crit}} = 3H^2/8\pi G$. We express the present value of Hubble's constant as $H(z=0) = H_0 = 100\, h$ km s$^{-1}$ Mpc$^{-1}$.

innermost ∼200 particles, provided that other numerical parameters are chosen wisely. Ghigna et al. (2000) suggest an additional convergence criterion based on the gravitational softening length scale, and argue that convergence is only achieved on scales that contain many particles and that are larger than about three times the scale where pairwise forces become Newtonian. Understanding the origin of such disparate conclusions and the precise role of numerical parameters is clearly needed before a firm theoretical prediction for the structure of CDM haloes on ∼kpc scales may emerge.

Motivated by this, we have undertaken a large series of numerical simulations designed to clarify the role of numerical parameters on the structure of simulated CDM haloes. In particular, we would like to answer the following question: what regions of a simulated dark matter halo in virial equilibrium can be considered reliably resolved? This question is particularly difficult because of the lack of a theory with which the true structure of dark haloes may be predicted analytically, so the best we can do is to establish the conditions under which the structure of a simulated dark halo is independent of numerical parameters. This is the question which we endeavour to answer in this paper.

There is a long list of considerations and numerical parameters that may influence the structure of simulated dark haloes:

(i)  the *N*-body code itself;
(ii)  the procedure for generating initial conditions;
(iii)  the accuracy of the force computation;
(iv)  the integration scheme;
(v)  the initial redshift;
(vi)  the time-stepping choice;
(vii)  the gravitational softening;
(viii)  the particle number.

Clearly the list could be substantially longer, but the items above are widely considered the most important concerning the structure of simulated dark haloes. Before we proceed to analyse their role, we must decide which properties of a dark matter halo we will assess for numerical convergence. Because, as mentioned above, disc galaxy rotation curves seem to pose at present one of the most pressing challenges to the CDM paradigm on small scales, we have decided to concentrate on the spherically averaged mass profile, as measured by the radial dependence of the circular velocity, $V_c(r) = \sqrt{GM(r)/r}$, or, equivalently, by the inner mean density profile, $\bar{\rho}(r) = 3M(r)/4\pi r^3$.

We note that the convergence criteria derived here apply strictly only to these properties, and that others, such as the three-dimensional shape of haloes, their detailed orbital structure, or the mass function of substructure haloes, may require different convergence criteria.

The basic philosophy of our convergence testing procedure is to select a small sample of haloes from a cosmological simulation of a large periodic box and to resimulate them varying systematically the parameters listed above, searching for regions in parameter space where the circular velocity curves are independent of the value of the numerical parameters, down to the smallest scales where Poisson uncertainties become important, i.e. roughly down to the radius that contains ∼100 particles.

Overall, this is a fairly technical paper of interest mostly to practitioners of cosmological *N*-body simulations. Readers less interested in numerical details may wish to skip to Section 6, where we discuss in detail the converged inner mass profile of the galaxy-sized ΛCDM halo used in our convergence study. The more technical sections include:

(i)  a discussion of the *N*-body codes used in this work, initial conditions set-up, and analysis procedure (Section 7 and the Appendix);

(ii)  a general discussion of the consequences of discreteness effects on simulations of dark matter haloes, including a derivation of 'optimal' choices (for given particle number) of the time-step and the gravitational softening (Section 3);

(iii)  a comparison between single- and multi-time-stepping techniques (Section 4);

(iv)  a discussion of the role of the gravitational softening, the initial redshift, the force accuracy, and the particle number on the inner mass profile of simulated haloes (Section 5);

Finally, a worked example of how to choose optimal parameters for a high-resolution simulation is presented in Section 5.5. We summarize our main conclusions in Section 7.

## 2  NUMERICAL METHODS

### 2.1  *N*-body codes

Most simulations reported in this paper have been performed with the parallel *N*-body code GADGET, written by Volker Springel, and available from http://www.mpa-garching.mpg.de/gadget (Springel, Yoshida & White 2001). In order to test the dependence of our results on the particular algorithmic choices made in GADGET, we have also used PKDGRAV, a code written by Joachim Stadel and Thomas Quinn (Stadel 2001). As we discuss in Sections 3 and 5, the two codes give approximately the same results for appropriate choices of the numerical parameters. We have not attempted to carry out a detailed comparison of the relative efficiency or speed of the codes; such a comparison is heavily dependent on the particular architecture of the hardware used, and on a variety of optimization and tuning procedures. We do note, however, that neither code seems obviously to outperform the other when our strict numerical convergence criteria are met.

The two *N*-body codes share a number of similarities. They both evaluate accelerations ('forces') on individual particles as a result of all others using a hierarchical tree data structure (Barnes & Hut 1986; Jernigan & Porter 1989), and (optionally) use individually adaptive time-stepping schemes to advance the integration of each particle. Periodic boundary conditions are handled in both codes via Ewald's summation technique (Hernquist, Bouchet & Suto 1991), although the implementation of the algorithm in each code is different.

Gravitational softening is introduced in the form of a 'spline' mass distribution [see, for example, Hernquist & Katz (1989) and Navarro & White (1993)] which, unlike the more traditional 'Plummer' softening of the early generation of *N*-body codes [see, for example, Aarseth (1985)], converges for pairwise interactions exactly to the Newtonian regime at a finite radius. The length scale of the spline kernel, $\epsilon_i$, can be chosen individually for each particle in PKDGRAV. GADGET, on the other hand, allows for different softenings to be chosen for up to six different particle 'species'. We quote the values of $\epsilon_i$ so that gravitational interactions between two particles are fully Newtonian for separations larger than $2\epsilon_i$.

The codes differ substantially in their implementation of the tree construction, in the force-evaluation algorithms and in the integrator scheme. Whereas PKDGRAV uses a spatial binary tree for gravity calculations, GADGET uses a version of the Barnes–Hut geometric oct-tree. Distant tree-node contributions to the force calculations include up to quadrupole expansion terms in GADGET, but up to hexadecapole in PKDGRAV. The tree is rebuilt every time-step in the

version of PKDGRAV that we tested (although this is not the case in the most up-to-date version), whereas we rebuild the tree in GADGET dynamically after $\sim 0.1 N_{tot}$ force computations since the last full reconstruction. ($N_{tot}$ is the total number of particles in the simulation.)

Finally, GADGET uses a simple second-order DKD (drift–kick–drift) leap-frog integrator scheme with the expansion factor as the integration variable, whereas PKDGRAV adopts a cosmic time-based KDK (kick–drift–kick) algorithm. All integrations are carried out in comoving coordinates. Details of these codes may be found in Springel et al. (2001), and in Stadel (2001). In the following subsections, we describe the numerical set-up used for the two codes. All simulations have been run on the IBM-SP supercomputer facilities at the University of Victoria (Canada), and on the T3Es at the Edinburgh Parallel Computer Centre (UK) and at the Max-Planck Rechenzentrum in Garching (Germany).

### 2.1.1 GADGET

GADGET has been the main simulation code used in this study, and it evolved as the project unfolded from the first public release v1.0 to the latest available release v1.1. All of the results presented here have been obtained with the latest version of the code.

GADGET presents the user with a number of options regarding time-stepping choices and the accuracy of the force calculations. In all cases we have used the tree-node-opening criterion recommended by Springel et al. (2001), where a Barnes–Hut opening criterion with $\theta = 0.6$ is used for the first force computation and a dynamical updating criterion is used subsequently. In this criterion, a node is opened if $Ml^4 > f_{acc} a_{old} r^6$, where $M$ is the mass of the node, $l$ is the node-side length, and $a_{old}$ is the acceleration that the particle experienced in the previous time-step. The parameter $f_{acc}$ (called ErrTolForceAcc in GADGET's parameter list) is set to $10^{-3}$ in our standard calculations. This condition can be overridden if the – DBMAX compile-time flag is activated. Enabling this flag imposes an additional condition for node-opening: multipole expansion of a node is only used if, in addition to the previous condition, the particle is *guaranteed* to lie outside the geometric boundaries of the node in question.[2] The results reported in Section 5.3 indicate that these choices are important to ensure convergence; resolving the inner structure of dark haloes requires highly accurate forces.

GADGET uses an integrator with completely flexible time-steps. The code carries, for each particle, a time, $t_i$, position, $\boldsymbol{r}_i$, velocity, $\boldsymbol{v}_i$, acceleration, $\boldsymbol{a}_i$, gravitational softening, $\epsilon_i$, and, optionally, a local density, $\rho_i$, and a local one-dimensional velocity dispersion, $\sigma_i$. From these quantities, time-steps, $\Delta t_i$, can be computed for each particle according to several possible choices:

$$\Delta t_i = \begin{cases} \eta_{a\epsilon} \sqrt{\epsilon_i/a_i}, & \text{if DtCrit} = 0; \\ \eta_a/a_i, & \text{if DtCrit} = 1; \\ \eta_{a\sigma}(\sigma_i/a_i), & \text{if DtCrit} = 2; \\ \eta_\rho (G\rho_i)^{-1/2}, & \text{if DtCrit} = 3; \\ \eta_{\sigma\rho} \min\left[(G\rho_i)^{-1/2}, (\sigma_i/a_i)\right], & \text{if DtCrit} = 4, \end{cases} \qquad (2)$$

where DtCrit refers to the runtime input parameter ErrTolIntAccuracy in GADGET, and $\eta$ is a dimensionless constant that controls the size of the time-steps (except for $\eta_a$, which has dimensions of velocity).[3] For ease of reference, we shall refer to the various choices for DtCrit using the following mnemonic shorthand: EpsAcc for DtCrit

= 0; VelAcc for DtCrit = 1; SgAcc for DtCrit = 2; SqrtRho for DtCrit = 3; and RhoSgAcc for DtCrit = 4, respectively.

We report below results obtained with several of these choices. Unless specified, a maximum time-step was imposed so that all particles took *at least* 200 time-steps during the whole integration. In practice, this limit affects a very small fraction of the particles in a typical run; resolving the inner structure of dark haloes requires typically several thousand time-steps.

### 2.1.2 PKDGRAV

In the PKDGRAV runs reported here, we have only explored variations in two parameters: the time-stepping parameter, $\eta$, and the gravitational softening, $\epsilon_i$. We note, however, that PKDGRAV is a very flexible code that includes a number of choices for the integrator scheme and time-stepping, and we have by no means explored all of its options. PKDGRAV was mainly used in this study to verify that the results obtained with GADGET are independent of the code utilized.

All PKDGRAV simulations that used individual time-steps were evolved to $z = 0$ using 50 system time-steps. The system time-step, $\Delta T$, is the maximum allowed for any particle. Individual particle time-steps are binned in a hierarchy so that $\Delta t_i = \Delta T/2^n$, where $n$ was allowed to take any value in the range (0, 20). This allows particles to take up to $\sim 10^8$ time-steps in a run, which means that in practice no significant restrictions have been placed on the minimum time-step.

Individual particle time-steps were chosen in PKDGRAV runs in a manner analogous to GADGET's EpsAcc criterion, i.e. $\Delta t_i \leqslant \eta \sqrt{\epsilon_i/a_i}$, although quantitatively accelerations differ because of the choice of integration variables. The parameter $\eta$ specifies the size of the time-steps and, consequently, the overall time accuracy of the integration. Finally, the force accuracy in PKDGRAV is controlled by , a redshift-dependent node-opening criterion. We have chosen for all runs $\theta = 0.55 (z > 2)$ and $\theta = 0.7$ for $z < 2$.

## 2.2 The initial conditions

Setting up initial conditions that faithfully represent the cosmogony we wish to investigate is a *crucial* step in the simulation process and, despite the popularity of cosmological $N$-body simulations, there is surprisingly little detail in the literature regarding how this is tackled by different groups. The major references on this topic in the refereed literature are the work of Efstathiou et al. (1985) and the recent papers by Bertschinger & Gelb (1991), Pen (1997), and by Bertschinger (2001); see also http://arcturus.mit.edu/cosmics and http://arcturus.mit.edu/grafic.

Our particular procedure follows closely that described in Efstathiou et al. (1985) and is described in detail in the Appendix. It aims to provide a particle realization of a Gaussian density field with the chosen primordial power spectrum, $P(k)$, on scales and at redshifts where linear theory is applicable.

We adopt the ΛCDM cosmological model, a low-density universe of flat geometry whose dynamics is dominated at present by a cosmological constant, $\Omega_0 = 0.3$, $\Omega_\Lambda = 0.7$ and $h = 0.65$. We assume that the initial power spectrum is Harrison–Zel'dovich ($P(k) \propto k$), modified by an appropriate cosmological transfer function, $T(k)$. For ΛCDM simulations we have chosen to use the analytical representation of the transfer function proposed by Bardeen et al. (1986) with shape parameter $\Gamma = 0.2$.

Our simulations proceed in two stages. First, a large, low-resolution, periodic box is run to $z = 0$ and used to select haloes

---

[2] A similar condition is activated by default in PKDGRAV.

[3] For convenience we have defined $\eta_{a\epsilon}$ to be directly proportional to the size of the time-step in all cases. For DtCrit = 0, $\eta_{a\epsilon}^2 = 2 \times$ ErrTolIntAccuracy.
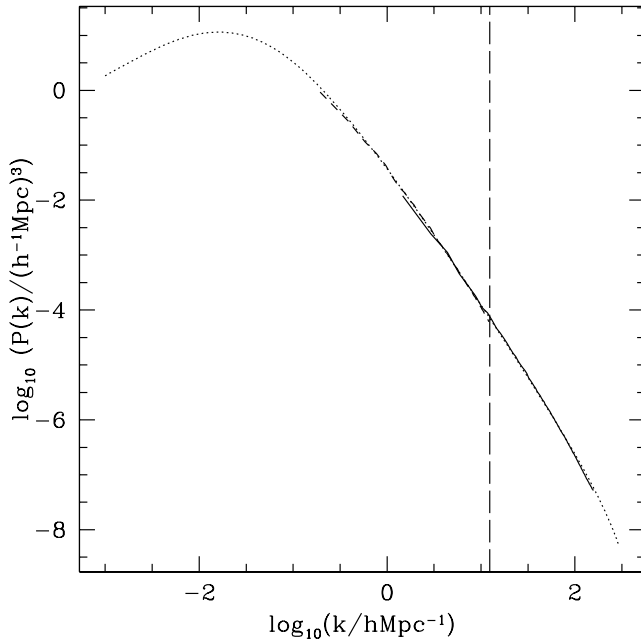
**Figure 1.** The dotted curve shows the theoretical $\Lambda$CDM power spectrum at redshift $z = 49$. The short dashed curve shows the measured power spectrum from the initial conditions of the parent simulation ($L_{box} = 32.5\,h^{-1}$ Mpc, $N_{box} = 128^3$). The solid line shows the power spectrum within the high-resolution box selected for resimulation ($L_{sbox} = 5.08\,h^{-1}$ Mpc, $N_{sbox} = 256^3$). The agreement with the theoretical power spectrum is good over nearly three orders of magnitude in wavenumber and seven decades in amplitude. Significant departures are expected for both curves at low $k$ as the number of long-wavelength modes is small. The charge assignment scheme causes a small drop at high-$k$ for both curves. The vertical long dashed line marks the scale in the resimulated initial conditions which corresponds to the transition between the long waves that are present with the same phase and amplitude as the parent simulation and the additional short waves added to improve the resolution. See the Appendix for more details of the computation of the power spectrum.

targeted for resimulation at much higher resolution (consult the Appendix for details). For the first step, we have generated a Fourier representation of the fluctuation distribution on a $128^3$ mesh and we have computed displacements for $128^3$ particles initially arranged on a cubic grid. The displacements assume an initial redshift of $z_i = 49$ in the $\Lambda$CDM cosmogony and are normalized so that at $z = 0$ the linear rms amplitude of mass fluctuations on spheres of radius $8\,h^{-1}$ Mpc is $\sigma_8 = 0.9$. The size of the box is $L_{box} = 32.5\,h^{-1}$ Mpc (co-moving), and the particle mass is $m_p = 4.55 \times 10^9 \Omega_0\,h^{-1}$ M$_\odot$. The dashed curve in Fig. 1 shows that the power spectrum computed from the displaced positions of the $128^3$ particles within this box is in very good agreement with the theoretical power spectrum (dotted curve).

The second stage of the procedure to generate initial conditions involves selecting a small region within the large periodic box destined to collapse into a halo selected for resimulation at higher resolution. In the case we consider here, this region is a box of $L_{sbox} = 5.08\,h^{-1}$ Mpc on a side. The advantage of this procedure is that we can in principle include many more particles in the high-resolution box than were present in the parent simulation (we use $N_{sbox} = 256^3$ in the case we consider here, giving a highest-resolution particle mass of $6.5 \times 10^5\,h^{-1}$ M$_\odot$). A new Fourier representation of the theoretical power spectrum is then generated, retaining the phases and amplitudes of the Fourier components in the parent simulation and

adding waves of higher frequency, periodic in the high-resolution box, up to the Nyquist frequency of the high-resolution particle grid. The solid line in Fig. 1 shows that the power spectrum measured directly from particle displacements in the high-resolution box is again in good agreement with the theoretical expectation.

Fig. 1 thus demonstrates that the power spectrum is reproduced well by both the parent simulation and the resimulated region. Altogether, the power spectrum is fit well over nearly three decades in wavenumber and seven decades in power. The maximum difference between the theoretical power spectrum and the measured power spectra is less than 0.05 dex, except at low wavenumbers where the small number of modes makes the variance of the measurement large.

Outside the high-resolution box, we resample the particle distribution in the parent simulation in order to provide for the tidal forces which act on the high-resolution particles. The resampling procedure bins particles into cells whose sizes vary approximately in proportion to their distance from the high-resolution patch, greatly reducing the total number of tidal particles needed to represent the tidal field. Not all particles in the high-resolution box will end up near the system of interest, so the location on the original grid of selected particles is used to identify an 'amoeba-shaped' region within the cube that is retained at full resolution. Regions exterior to the 'amoeba' are coarse sampled with particles of mass increasing with distance from the region of interest (Fig. 2).

## 2.3 The simulations

The initial conditions file containing the displacement field for $N_{sbox} = 256^3$ particles generated in the way described above can be easily rescaled to generate realizations of each system with varying
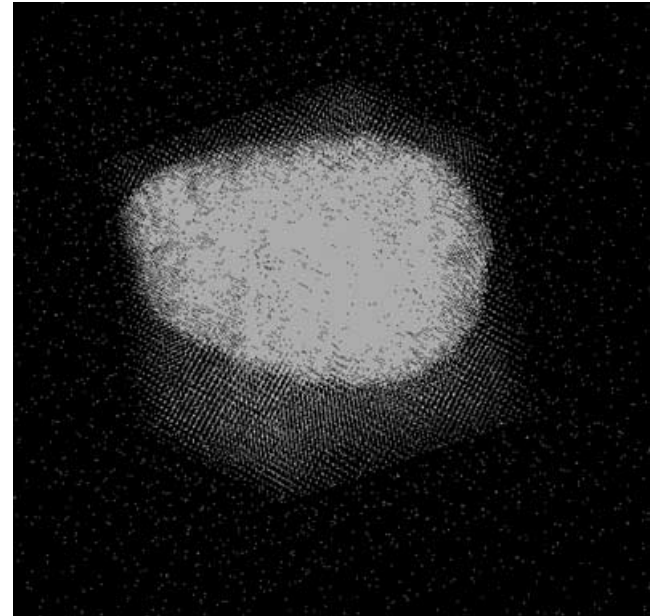


**Figure 2.** Particle distribution in the initial conditions of our $128^3$ runs at $z_i = 49$. Clearly seen is the 'amoeba'-shaped region containing the highest-resolution particles, which is embedded within the $5.08\,h^{-1}$ Mpc high-resolution cube used for the resimulation. Beyond the boundaries of the high-resolution cube lie massive particles that coarsely sample the entire volume of the $32.5\,h^{-1}$ Mpc periodic box. This figure is in colour on *Synergy*, the online version of the journal.

**Table 1.** Properties of the simulated halo.

| Label | $r_{200}$ ($h^{-1}$ kpc) | $V_{200}$ (km s$^{-1}$) | $M_{200}$ ($10^{10}$ M$_\odot$) | $N_{\text{sbox}}$ | $N_{200}$ | $\epsilon_{\text{acc}}$ ($h^{-1}$ kpc) | $\epsilon_{\text{opt}}$ ($h^{-1}$ kpc) |
|---|---|---|---|---|---|---|---|
| Halo 1 | 205 | 205 | 200 | $256^3$ | $3.17 \times 10^6$ | 0.12 | 0.46 |
| | | | | $128^3$ | $3.97 \times 10^5$ | 0.33 | 1.30 |
| | | | | $64^3$ | $4.96 \times 10^4$ | 0.92 | 3.68 |
| | | | | $32^3$ | $6.20 \times 10^3$ | 2.60 | 10.40 |

particle number or starting redshift. To modify the starting redshift, we simply rescale the displacements and velocities according to the linear growth factor. To reduce the particle number, we average successively displacements in the high-resolution box over eight neighbouring cubic cells. We refer to these 'reduced' initial conditions using the total number of particles in the high-resolution box: $256^3$, $128^3$, $64^3$ and $32^3$, respectively (Table 1).

These realizations may be used to test how numerical parameters affect the equilibrium structure of the dark halo at $z = 0$. Because runs with $32^3$ particles are relatively inexpensive, we have used them for a large series of simulations varying systematically all the numerical parameters under scrutiny. This series (which contains several hundred runs) allows us to survey the large available parameter space and to draw preliminary convergence criteria that are then confirmed with a series of runs with $64^3$ particles. The $128^3$ and $256^3$ simulations are too expensive to allow a full convergence study, so fewer of them were carried out, typically using values of the numerical parameters close to convergence. These are used mainly to test the dependence of our results on the total number of particles in the simulations.

## 2.4 The halo

We concentrate our analysis on a single halo selected from our sample, although similar runs on two other haloes confirm the conclusions presented here. The mass accretion history of this system is presented in Fig. 3. The halo accretes half of its present-day mass by $z \approx 0.66$ (expansion factor $a = 0.6$), when it undergoes a major merger. The last significant merger event occurs at $z \approx 0.4$ ($a = 0.71$), when the system accretes the last 20 per cent of its final mass. After this, the system remains relatively undisturbed, and by $z = 0$ it is close to virial equilibrium. The virial radius, also shown in Fig. 3, changes by less than 7 per cent after $z \approx 0.4$. The mass in the inner regions of the halo is assembled much earlier. Half of it is already in place by $z \approx 5$ ($a \approx 0.17$) and after $z \sim 1$ substantial fluctuations occur only during major mergers. (See the triangles in Fig. 3, which track the mass in the innermost 20 (physical) kpc.)

## 2.5 The analysis

We focus our analysis on the spherically averaged mass profile at $z = 0$. This is measured by sorting particles in distance from the centre and binning them in groups of 100 particles each. The cumulative mass within these bins, $M(r)$, is then used to compute the circular velocity profile of each halo, $V_c(r) = \sqrt{GM(r)/r}$, and the cumulative density profile, $\bar{\rho}(r) = 3M(r)/4\pi r^3$, which we use in our analysis.

It is important to choose carefully the halo centre, especially as the haloes are not spherically symmetric. The centre of each halo is
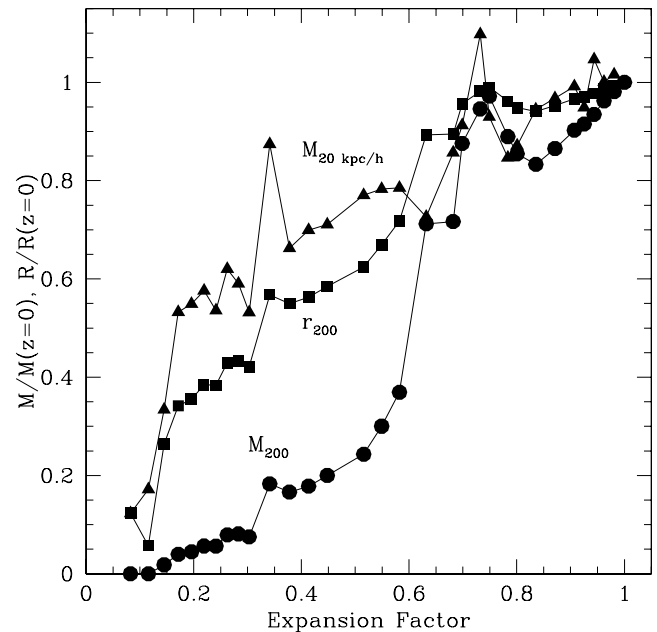


**Figure 3.** Evolution of the virial radius of the main progenitor of the system, $r_{200}$, of the mass contained within that radius, $M_{200}$, and of the mass within the innermost $20\,h^{-1}$ (physical) kpc. Data are normalized to values at the present day. For the virial radius, the ratio of the values in *comoving* units is shown. The system undergoes its last major merger at $z \sim 0.66$, accretes little mass afterwards and is close to virial equilibrium at $z = 0$. The mass within the inner $20\,h^{-1}$ kpc is assembled earlier than the rest, and is only affected seriously during major mergers. This figure is in colour on *Synergy*, the online version of the journal.

determined using an iterative technique in which the centre of mass of particles within a shrinking sphere is computed recursively until a convergence criterion is met. At each step of the iteration, the centre of the sphere is reset to the last computed barycentre and the radius of the sphere is reduced by 2.5 per cent. The iteration is stopped when a specified number of particles (typically either 1000 particles or 1 per cent of the particles within the high-resolution region, whichever is smaller) is reached within the sphere. Halo centres identified with this procedure are quite independent of the parameters chosen to initiate the iteration, provided that the initial sphere is large enough to encompass a large fraction of the system. In a multi-component system, such as a dark halo with substructure, this procedure isolates the densest region within the largest subcomponent. In more regular systems, the centre so obtained is in good agreement with centres obtained by weighing the centre of mass by the local density or gravitational potential of each particle. We have explicitly checked that none of the results presented here are biased by our particular choice of centring procedure.

# 3 THE RELATIONSHIP BETWEEN PARTICLE NUMBER, SOFTENING AND TIME-STEP

The main goal of this study is to identify the conditions under which the structure of simulated haloes, in particular their circular velocity profile, is independent of numerical parameters. We start with a brief discussion of the relationship between three of the main parameters: the number of particles, $N$; the gravitational softening, $\epsilon$; and the time-step, $\Delta t$ (Section 3.1). We proceed then (Section 3.2) to verify numerically the scalings expected between these quantities through a series of runs where the time-step for all particles is kept fixed and constant throughout the evolution.

## 3.1 Analytic estimates

Modelling the formation of dark matter haloes with $N$-body simulations entails a number of compromises dictated by limited computing resources. The choice of particle number, time-step and gravitational softening may all affect, in principle, the reliability of the structure of simulated haloes. We explore here the various limitations imposed by these numerical parameters. The analysis assumes, for simplicity: a steady-state system with circular speed, $V_c(r)$; enclosed mass, $M(r) = r V_c(r)^2/G$; enclosed particle number, $N(r)$; and orbital time-scale, $t_{circ} = 2\pi r/V_c$. The specific energy of a typical orbit at radius $r$ is $E(r) \approx v^2 \approx V_c(r)^2$.

### 3.1.1 N and collisional relaxation

When a finite number of particles is used to represent a system, individual particle accelerations will inevitably deviate from the mean-field value when particles pass close to each other. Even when orbits are integrated with perfect accuracy, these 'collisions' lead to changes of the order of unity in energy on the relaxation time-scale [see, for example, Binney & Tremaine (1987)]

$$\frac{t_{relax}}{t_{circ}} \sim \frac{N(r)}{\ln(r/\epsilon)}. \tag{3}$$

Thus, energy changes because of two-body effects after integration time $t_0$ are given by

$$\frac{\delta E}{E} \sim \left(\frac{t_0}{t_{relax}}\right)^{1/2} \sim \left(\frac{t_0}{t_{circ}(r)} \frac{\ln(r/\epsilon)}{N(r)}\right)^{1/2}. \tag{4}$$

Two-body effects first become important in the inner core of the system. Suppressing these effects is primarily a condition on the number of particles and depends only weakly on $\epsilon$. The time-step, of course, does not appear explicitly in this criterion. We return to the limitations imposed by collisional relaxation in Section 5.4.

### 3.1.2 Time-step and integration accuracy

Accurate integration of the equations of motion of dark matter particles requires a careful choice of the time-step adopted to evolve the system. A second-order accurate integration with time-step $\Delta t$ induces a relative error in position, velocity and energy, which scales as

$$\frac{\delta r}{r} \propto \frac{\delta v}{v} \propto \frac{\delta E}{E} \propto \left(\frac{v\Delta t}{r}\right)^3 \propto \left(\frac{\Delta t}{t_{circ}}\right)^3. \tag{5}$$

Note that this error depends only on the size of $\Delta t$, and that it is independent of $N$ and of $\epsilon$, consistent with our assumption of a smooth, collisionless system.

If errors on subsequent time-steps add incoherently, then the error at the end of a total integration time, $t_0$, is

$$\frac{\delta E}{E} \propto \left(\frac{t_0}{\Delta t}\right)^{1/2} \left(\frac{\Delta t}{t_{circ}}\right)^3 \propto \frac{(t_0 \Delta t^5)^{1/2}}{t_{circ}^3}. \tag{6}$$

For a given $\Delta t$, then, we expect orbits to be reliably modelled only at radii exceeding a certain value $r_{conv}$ defined by

$$\frac{t_{circ}(r_{conv})}{t_0} \propto \left(\frac{\Delta t}{t_0}\right)^{5/6}. \tag{7}$$

### 3.1.3 Time-step and discreteness effects

Finite-$N$ systems are not smooth, and errors in the integration will also occur during close encounters between particles. The effects of such encounters will be incorrectly treated by the simple integrators used in PKDGRAV and GADGET whenever the predicted separation at mid-step between a particle and a near neighbour satisfies $|s| = s < v\Delta t$. The error in velocity at the end of the step induced by this 'unexpected' encounter is then

$$\delta v \sim \Delta t \frac{Gms}{(s^2 + \epsilon^2)^{3/2}} \tag{8}$$

assuming Plummer softening. Such encounters occur with probability

$$p(s)\,ds \sim 4\pi \; s^2\,ds \, \frac{\rho}{m} \sim \frac{s^2}{r^2} \frac{ds}{Gm/v^2} \tag{9}$$

where $\rho$ is the mean matter density at the point of encounter, and $m$ is the particle mass. The maximum possible size of this error is

$$(\delta v)_{max} \sim \frac{Gm\Delta t}{\epsilon^2}. \tag{10}$$

The average velocity change obtained by integrating equation (8) over the particle distribution is just that due to the mean density field of the system. However, averaging the specific energy change over the discrete particle distribution gives a positive second-order contribution in excess of that expected along the mean-field orbit. For a single step,

$$\delta E \sim \frac{Gm\Delta t^2}{\epsilon r^2} \tag{11}$$

where the simplification arises because the integral is dominated strongly by contributions at $s \sim \epsilon$. After integration time $t_0$, the total energy change is then

$$\frac{\delta E}{E} \sim \frac{t_0}{\Delta t} \frac{Gm\Delta t^2}{\epsilon r^2} \sim \frac{1}{N(r)} \frac{r}{\epsilon} \frac{t_0 \Delta t}{t_{circ}^2}. \tag{12}$$

For a given $\Delta t$, then, we expect orbits to be reliably modelled at radii larger than a certain $r_{conv}$ defined by the following condition

$$\frac{t_{circ}(r_{conv})}{t_0} \approx \left(\frac{\Delta t}{t_0}\right)^{1/2} \frac{(Gm/\epsilon)^{1/2}}{V_c(r_{conv})}. \tag{13}$$

Because $V_c$ does not change dramatically with radius in CDM haloes, we see by comparing equation (7) with equation (13) that, in the presence of discreteness effects, the number of time-steps required for convergence increases as $\epsilon^{-1}$. Economy reasons thus dictate the use of large softenings to minimize the number of time-steps. On the other hand, large softenings compromise the spatial resolution of the simulations. These competing effects suggest the existence of an 'optimal' softening choice, $\epsilon_{opt}$, which maximizes resolution whilst at the same time avoiding discreteness effects and thus minimizing the number of time-steps required. We turn our attention to the softening next.

### 3.1.4 Softening and discreteness effects

When accelerations are softened, the *maximum* stochastic acceleration that can be caused by close approach to an individual particle is roughly $a_{m\epsilon} = Gm/\epsilon^2$, where $m$ denotes the particle mass. It is useful to compare this with the *minimum* mean-field acceleration, which occurs at the outer (virial) radius of the system, $a_{min} \approx GM_{200}/r_{200}^2$. The condition $a_{m\epsilon} \lesssim a_{min}$ sets a lower limit to the softening needed to prevent strong discreteness effects,

$$\epsilon > \epsilon_{acc} \approx \frac{r_{200}}{\sqrt{N_{200}}}, \tag{14}$$

where $N_{200} = M_{200}/m$ is the total number of particles within $r_{200}$. When this condition is satisfied, discreteness causes only small changes in particle accelerations, and so does not significantly affect the time-stepping in integration schemes with an acceleration-based time-step criterion.

Note that this condition is typically more restrictive than the usual requirement that large-angle deflections be prevented during two-body encounters. The latter is given by $\epsilon > \epsilon_{2b} = Gm/\sigma^2$, where $\sigma$ is the characteristic velocity dispersion of the system (White 1979). Because $\sigma^2 \approx GM_{200}/2r_{200} = GmN_{200}/2r_{200}$, then this condition requires that forces be softened on scales smaller than $\epsilon_{2b} \approx 2r_{200}/N_{200}$, which is usually smaller than $\epsilon_{acc}$. In Section 3.2, we determine empirically the relationship between $\epsilon_{acc}$ and the 'optimal softening' $\epsilon_{opt}$ referred to in Section 3.1.3.

### 3.2 Runs with constant time-step

In order to validate the scalings derived in the previous subsection and to determine empirically the optimum values of the softening and time-step, we have carried out a series of convergence tests where the time-step has been kept constant and is shared by all particles. Disabling the multi-time-stepping capabilities of the codes allows us to concentrate on the role of the time-step size, rather than on the virtues or shortcomings of scaling it in various ways for individual particles.

The structure of the dark matter halo chosen for our study at $z = 0$ is illustrated in Fig. 4, where we show the circular orbit time-scale, $t_{circ}(r) = 2\pi r/V_c(r)$, as a function of radius. Time-scales are measured in units of $t_{circ}(r_{200}) = 0.2\pi H_0^{-1}$, which is of the order of the age of the Universe, $t_0$. Radii are measured in units of the virial radius, $r_{200} \approx 205\,h^{-1}$ kpc. The gravitational softening, shown by a vertical dotted line, was kept constant in these runs, which had $128^3$ high-resolution particles ($\sim 4 \times 10^5$ within $r_{200}$) and were run with PKDGRAV. The innermost point plotted in each curve corresponds to the radius that contains 100 particles. From top to bottom, the curves in Fig. 4 illustrate how the mass profile of the simulated halo changes as the total number of time-steps increases, by successive factors of 2, from $N_{\Delta t} = 100$ (top curve) to $N_{\Delta t} = 6400$ (bottom dashed curve).

The halo becomes more centrally concentrated as $N_{\Delta t}$ increases, and approaches a 'converged' structure for $N_{\Delta t} \gtrsim 3200$. Runs with fewer time-steps than this still converge to the right mass profile but at increasingly larger radii. It is interesting to explore how the radius where convergence is achieved, $r_{conv}$, depends on the number of time-steps. We find $r_{conv}$ by identifying the radius at which systematic departures greater than 10 per cent in the circular time-scale profile first become noticeable, gauged against the run with the largest number of time-steps. This is easily read off the profiles presented in Fig. 4. Arrows in this figure indicate $t_{circ}(r_{conv})$ for each choice of $N_{\Delta t}$.
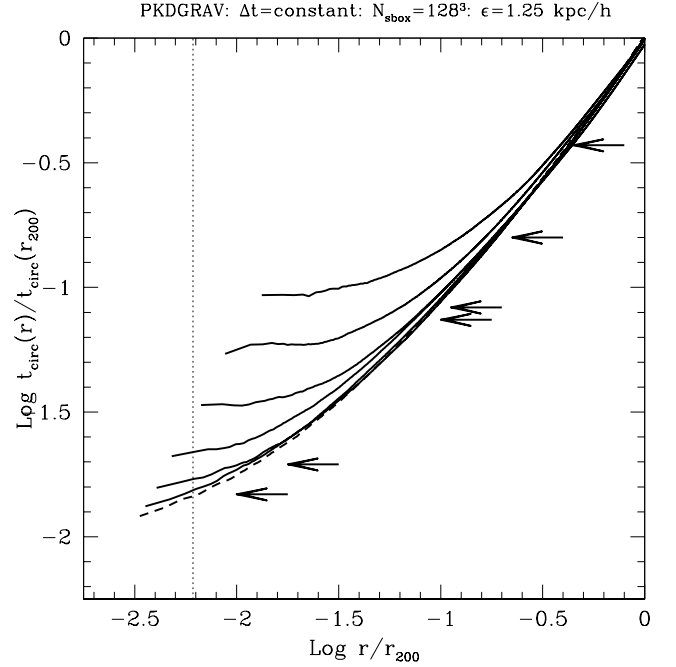


**Figure 4.** Circular orbit time-scale as a function of radius for a series of runs with constant time-step. All runs have $128^3$ particles within the high-resolution box, $\epsilon = 1.25\,h^{-1}$ kpc (shown by a dotted vertical line), and have been run with PKDGRAV. The total number of time-steps used in each run increases from the top down, from $N_{\Delta t} = 100$ to $N_{\Delta t} = 6400$ for the dashed curve at the bottom. From top to bottom, arrows mark the smallest radius where convergence, relative to the smallest-time-step run, is achieved in each case. This figure is in colour on *Synergy*, the online version of the journal.

The solid circles in Fig. 5 show the converged time-scales thus determined as a function of the size of the time-step. Converged circular times follow closely the $\Delta t^{5/6}$ dependence expected from equation (7), suggesting that the choice of softening in this series is such that discreteness effects are negligible. This is perhaps not surprising, as $\epsilon = 1.25$ kpc $h^{-1}$ is about four times larger than the lower limit estimated in equation (14), $\epsilon_{acc} = r_{200}/\sqrt{N_{200}} = 0.32$ kpc $h^{-1}$ (for $N_{sbox} = 128^3$).

The solid squares in Fig. 5 (left panel) correspond to the same exercise carried out for several choices of softening when the number of high-resolution particles is reduced to $64^3$. For the same softening, $\epsilon = 1.25$ kpc $h^{-1}$, achieving convergence with $64^3$ particles requires significantly smaller time-steps than with $128^3$, as expected, because discreteness effects become more important as the number of particles is reduced. It is also clear from Fig. 5 that the dependence of $t_{circ}(r_{conv})$ on $\Delta t$ changes as $\epsilon$ decreases, shifting gradually from $\Delta t^{5/6}$ to $\Delta t^{1/2}$. This transition is precisely what is expected from the analytical estimates in Section 3.1; see equations (7) and (13).

There is further supporting evidence in Fig. 5 for the validity of the analytical estimates. Consider, for example, the right panel, where we present the results of runs with $32^3$ high-resolution particles. The trends are similar to those in the left panel, but the transition to the discreteness-dominated regime ($t_{circ}(r_{conv}) \propto \Delta t^{1/2}$) occurs for even larger values of $\epsilon$.

It is possible to use these results to estimate the softening above which discreteness effects become unimportant for the various series. From Fig. 5, we find that, for $64^3$ particles, this 'optimal'
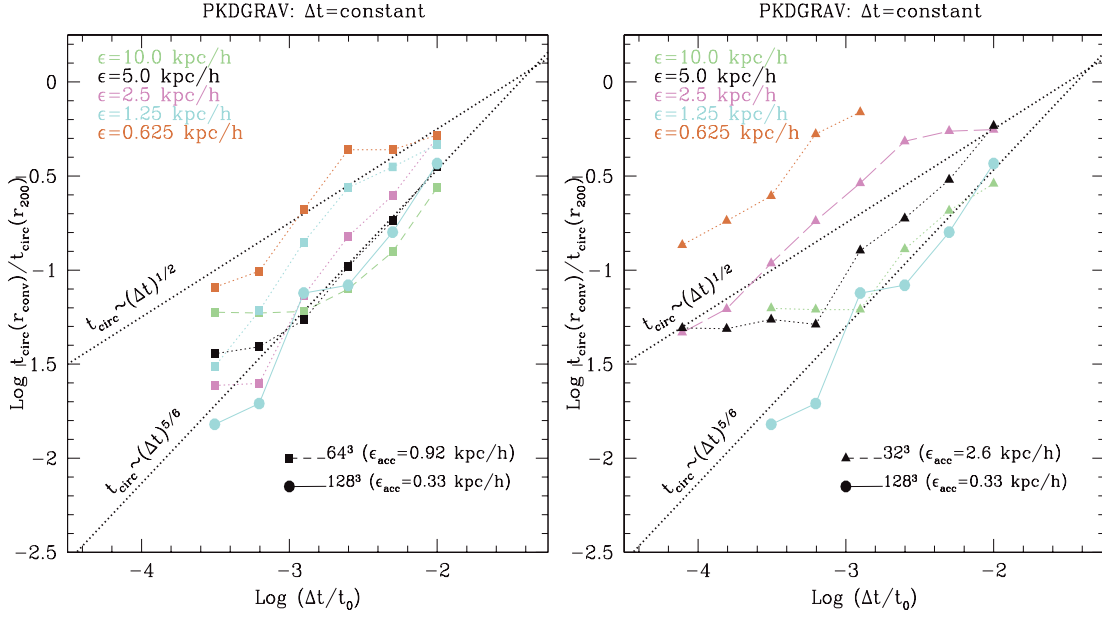
**Figure 5.** Circular orbit time-scale at the smallest 'converged' radius (as illustrated by arrows in Fig. 4) as a function of the time-step for PKDGRAV runs. The left panel shows the results for $N_{\rm sbox} = 64^3$; the right panel for $N_{\rm sbox} = 32^3$. In both panels, the results corresponding to $N_{\rm sbox} = 128^3$ are shown by solid circles. As the time-step decreases, the radii where the orbital time-scales are shorter become well resolved. This 'saturates' when the radius becomes comparable to the softening and flattens the curves horizontally in some cases. Note also that, as the softening is reduced, the number of time-steps required for convergence increases substantially. Refer to the text for a thorough discussion.

softening is somewhere between 2.5 and 5 kpc $h^{-1}$, while for $32^3$ particles it is of the order of $\sim 10$ kpc $h^{-1}$. Our $128^3$ runs suggest that $\epsilon_{\rm opt} \approx 1.25 \, h^{-1}$ kpc for this series. The optimal softening appears thus to scale with $N$ just as suggested by our discussion of equation (14). The simple empirical rule,

$$\epsilon_{\rm opt} \approx 4\epsilon_{\rm acc} = \frac{4r_{200}}{\sqrt{N_{200}}}, \tag{15}$$

appears to describe the numerical results well.

The reason why $\epsilon_{\rm opt}$ is about a factor of *4* larger than $\epsilon_{\rm acc}$ is likely to be related to the fact that, when softening is chosen to optimize results for haloes at $z = 0$, the choice is not optimal for their progenitors at earlier times. Indeed, $r_{200}(M, z) \propto (\Omega(z)/\Omega_0)^{1/3} M^{1/3} (1+z)^{-1}$, which implies that, for softenings fixed in comoving coordinates, $\epsilon/\epsilon_{\rm opt}(N, z) \propto N(z)^{1/6}$. Small-$N$ progenitors thus have smaller softenings than optimal and may be subject to discreteness effects. The dependence on the number of particles is weak, however, and it is possible that the factor of 4 in equation (15) may act as a 'safety factor' to ensure that discreteness effects are negligible at all times.

A number of other predictions from the analytical scalings presented in Section 3.1 are also confirmed by the data in Fig. 13. For example, when discreteness effects dominate, converged time-scales are expected to scale as $\epsilon^{-1/2}$ [equation (13)]. This is in good agreement with the results of the $32^3$-particle runs; for given time-step, $t_{\rm circ}(r_{\rm conv})$ is seen to increase by roughly a factor of *2* when $\epsilon$ decreases by a factor of 4, from $\epsilon = 2.5$ to 0.625 kpc $h^{-1}$.

Finally, the analytical estimates suggest that the time-step choice should be independent of $N$ and $\epsilon$ when discreteness effects are unimportant. This is also reproduced in the simulation series; for $\epsilon \gtrsim \epsilon_{\rm opt}$, all runs, independent of $N$, lie along the *same* dotted line that delineates the

$$t_{\rm circ}(r_{\rm conv}) \approx 15 \left( \frac{\Delta t}{t_0} \right)^{5/6} t_{\rm circ}(r_{200}) \tag{16}$$

scaling. This confirms that the size of the time-step is the most important variable when discreteness effects are unimportant; roughly 400, 7000 and 110 000 time-steps are needed to resolve regions where $t_{\rm circ}$ is, respectively, $\approx 10$ per cent, 1 per cent and 0.1 per cent of the orbital time-scale at the virial radius.

### 3.3 Convergence and integrator schemes

So far these conclusions are based on runs carried out with PKDGRAV. Are they general or do they depend on the particular choice of integrator scheme? We have explored this by performing a similar series of constant-time-step runs with GADGET, which uses a different integrator (Section 2.1). There is another difference between the GADGET series and that carried out with PKDGRAV; GADGET integrates the equations of motion using the expansion factor, $a$, as the time variable. Constant-time-step runs carried out with GADGET were therefore evolved using a fixed expansion-factor step, $\Delta a$. Comparing GADGET and PKDGRAV runs with the same *total* number of steps, GADGET takes shorter time-steps at high redshift, longer time-steps at moderate $z$ and similar time-steps at $z \approx 0$.

We compare the results of the two series in Fig. 6, where we plot, at $z = 0$, the radii containing various mass fractions of the halo as a function of the number of time-steps, $N_{\Delta t}$. The three series shown correspond to runs with $128^3$ high-resolution particles; two were run with GADGET and one with PKDGRAV. The choice of softening in each case is indicated in the figure labels. The four radii shown contain, from bottom to top, 0.025, 0.2, 1.6 and 12.8 per cent of the mass within $r_{200}$, respectively.

Convergence is approached gradually and monotonically in PKDGRAV runs (solid circles in Figs 5 and 6). For $N_{\Delta t} \sim 3200$,
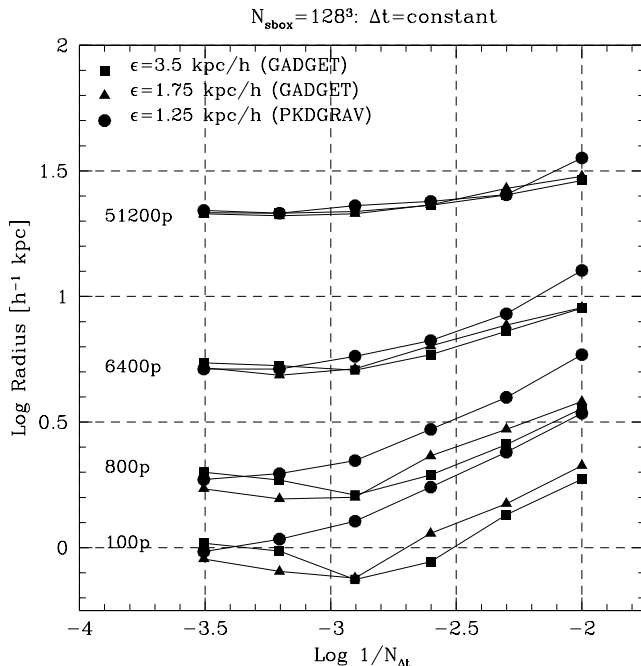
**Figure 6.** Radii enclosing various numbers of particles as a function of the total number of time-steps. The results shown correspond to runs with $128^3$ particles in the high-resolution box and were run with PKDGRAV and GADGET, as labelled. The PKDGRAV runs approach convergence progressively and monotonically. On the other hand, with poor time resolution GADGET can produce artificially dense 'cuspy' cores, most noticeable when $N_{\Delta t} = 800$. These 'cuspy cores' seem to be inherent to the integrator and stepping schemes chosen in GADGET. Note, however, that both codes need approximately the same number of time-steps for full convergence. This figure is in colour on *Synergy*, the online version of the journal.

convergence is achieved at all radii containing more than $\sim$100 particles; fewer time-steps are needed to converge at larger radii, as discussed in the previous subsection.

Convergence also occurs gradually, but *not* monotonically, in the case of GADGET (solid squares and triangles in Fig. 6). For the same number of steps, GADGET results typically in mass profiles that, near the centre, are more concentrated than those of PKDGRAV, as shown by the systematically smaller radii that contain the same mass fraction. The effect is particularly noticeable for $N_{\Delta t} \approx 800$, when the central density profile is actually *steeper* than the 'converged' result achieved for $N_{\Delta t} \gtrsim 3200$.

Further runs with different softenings and numbers of particles suggest that the presence of these 'cuspy cores' in systems evolved with poor time resolution is inherent to $\Delta a = $ constant GADGET runs, and is not just a fluke. On the other hand, the artificial cusps only occur in regions well inside the convergence criterion derived from the PKDGRAV series. Outside the convergence radius delineated by equation (16), both GADGET and PKDGRAV results appear safe. We can conclude that GADGET and PKDGRAV require approximately the same number of time-steps to resolve the whole system.

To summarize, the central densities of systems evolved with poor time resolution may be overestimated or underestimated, depending on the integrator scheme adopted. Such sensitivity to the integrator scheme emphasizes the vulnerability of the central regions to numerical artefact and the need for detailed convergence studies such as that presented here before firm conclusions can be reached regarding the inner density profiles of CDM haloes.

### 3.4 Summary

The agreement presented above between numerical results and analytical estimates gives us confidence that it is possible to achieve convergence in the mass profiles of simulated dark haloes down to scales which contain as few as 100 particles or where the gravitational softening starts to dominate. A few prescriptions for an efficient and accurate integration seem clear:

(i) choose gravitational softenings so that $\epsilon \gtrsim \epsilon_{\mathrm{opt}} = 4 r_{200}/\sqrt{N_{200}}$ [equation (15)] to minimize the number of time-steps needed; and

(ii) regard as converged only regions where circular orbit time-scales exceed $\approx 15(\Delta t / t_0)^{5/6} t_{\mathrm{circ}}(r_{200})$ [equation (16)].

One problem with these prescriptions is that, in a large cosmological $N$-body simulation, where systems of different mass and size form simultaneously, it is possible to choose optimal values of the numerical parameters only for systems of roughly the same mass. Also, resolving the inner density profiles, where orbital time-scales can reach a small fraction of the age of the Universe, may prove impractical with a constant time-step, as the number of time-steps is then dictated by the densest region of the system, which may contain only a small fraction of the total number of particles. It is therefore important to learn how the structure of simulated dark haloes is affected when non-optimal choices of numerical parameters are made as well as when multi-time-stepping integration techniques are adopted. We turn our attention to these topics in the following sections.

## 4 ADAPTIVE MULTI-STEPPING TECHNIQUES

In order to improve efficiency, many cosmological $N$-body codes use individual time-steps that can vary with time and from particle to particle. This allows the time integration scheme to adapt spatially so as to achieve high accuracy across the whole body of non-linear structures. The two codes used in this study, PKDGRAV and GADGET, can use individual time-steps, although, as discussed in Section 2.1, they differ significantly in the choice of integration scheme.

Evaluating the efficiency gain is not straightforward, because computing resources in most parallel environments do not scale in simple ways with the total number of particles and of time-steps, and the latter is ill-defined when individual adaptive time-steps are adopted. We assume, for simplicity, that the bulk of the computational work is invested in computing individual accelerations ('forces'), and we deem efficient time-stepping choices that achieve 'full convergence'[4] whilst minimizing the total number of force computations, $N_{\mathrm{ftot}}$.

For the integrators used in PKDGRAV and GADGET, forces are computed once every time the position (or velocity) of a particle is advanced, so that $\bar{N}_{\Delta t} = N_{\mathrm{ftot}}/N$ can be thought of as the average number of time-steps in a run. $N_{\mathrm{ftot}}$ is an imperfect measure of the total computational work, because it neglects the overhead that stems from tree construction, neighbour searching (if required by the time-stepping choice), synchronization, and communication between nodes, but is none the less a useful guide for assessing the efficiency of various time-stepping techniques.

---

[4] We use the term 'full convergence' when it extends down to the scale containing as few as 100 particles or gravitational softening, whichever is larger.
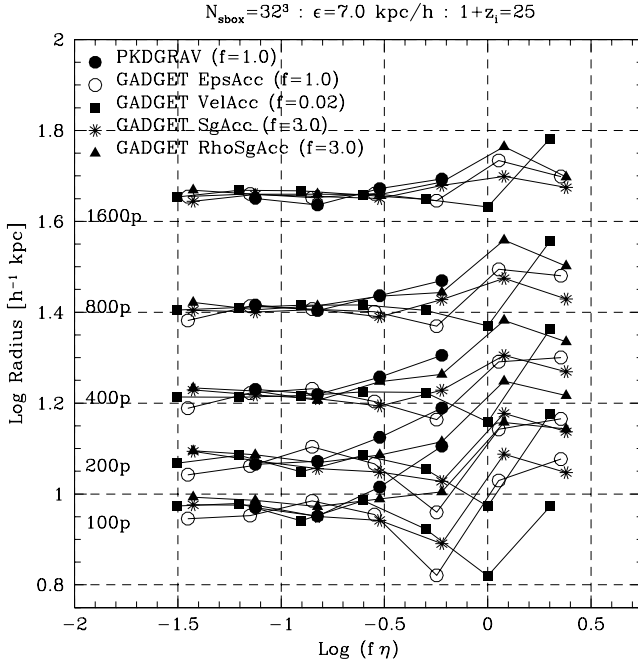
**Figure 7.** As Fig. 6, but for radii as a function of the time-stepping parameter, $\eta$. The number of time-steps decreases linearly with $\eta$ (Section 2). The values of $\eta$ shown in the figure have been scaled by an arbitrary factor, $f$, so that for given $f\eta$ all runs have a similar number of total force computations, $N_{\rm ftot}$. Values of $f$ are given in the figure labels. This figure is in colour on *Synergy*, the online version of the journal.

### 4.1 Comparison of time-step criteria

GADGET allows for five different ways of setting the time-step, and we have explored extensively four of these. Our main results are illustrated in Fig. 7, which is analogous to Fig. 6 but for runs with $32^3$ high-resolution particles. The radii shown enclose 1.6, 3.2, 6.5, 12.9 and 25.8 per cent of the mass within the virial radius, respectively, and are shown as a function of the time-step parameter, $\eta$ (Section 2.1.1). We adopt for this series a softening of $7\,h^{-1}$ kpc, close to the 'optimal' value for this number of particles (see Table 1). For convenience, we have scaled $\eta$ by an arbitrary factor $f$ (listed in the labels of Fig. 7) chosen so that, for given $f\eta$, all runs in this figure incur approximately the same total number of force computations. CPU consumption is lowest for EpsAcc and VelAcc, $\sim$25 per cent higher for SgAcc, and highest (by $\sim$60 per cent) for RhoSgAcc because the neighbour search required by the latter two criteria imposes a significant overhead.

The main conclusion to be drawn from Fig. 7 is that all time-stepping choices appear to converge for approximately the same value of $f\eta \lesssim 0.2$ or, equivalently, for the same $N_{\rm ftot}$. For $f\eta \approx 0.2$, $N_{\rm ftot} \approx 2.2 \times 10^7$, which implies that on average a minimum of $\sim$650 time-steps is required for full convergence. This is comparable to the number of *constant* time-steps needed for full convergence (see Fig. 5).

For $f\eta > 0.2$, deviations from convergence are obvious in all cases. Deviations are monotonic in the case of PKDGRAV and RhoS-gAcc runs; the densities at all radii increase gradually as the time-step decreases and converge for $f\eta \lesssim 0.2$. On the other hand, the behaviour of the inner mass profile in the case of other criteria is clearly non-monotonic; the central shells dip well below the converged value before bouncing back to convergence as $f\eta$ approaches

0.2. This is reminiscent of the artificially cuspy cores discussed in Section 3.3, but it seems to affect radii well beyond the softening.

Note that these artificial 'cuspy cores' affect runs with GADGET's EpsAcc criterion as well, which is formally the same as used in PKDGRAV. The monotonic approach to convergence seen in PKDGRAV runs thus suggests that the presence of 'cuspy cores' in runs with poor time resolution is an artefact related to GADGET's integrator scheme rather than to the time-stepping choice. Artificially cuspy cores are an undesirable feature in large cosmological simulations, because dense cores may survive the hierarchical assembly of structure and lead to artefacts in the density profiles of systems formed by the merger of affected progenitors. This type of subtle artefact again demonstrates that careful convergence studies of the type presented here are needed to guarantee that the inner mass profiles of dark matter haloes can be robustly measured in *N*-body simulations.

### 4.2 The dependence on softening

According to the analysis presented in Section 3.1, the time-step required for convergence is independent of the softening when discreteness effects are unimportant [i.e. when $\epsilon \gtrsim \epsilon_{\rm opt}$, see equation (7)] but should become increasingly short as $\epsilon$ decreases below the optimal value [see equation (13)]. Because optimal softenings can only be adopted for systems of roughly the same mass in a large cosmological simulation, optimizing the choice for massive clumps leads to less-than-optimal softenings in low-mass haloes. For such systems, keeping the values of $\eta$ found to give convergence in the last subsection (i.e. $f\eta \approx 0.2$ with the values of $f$ given in Fig. 7) may not guarantee convergence unless the time-stepping criterion scales appropriately with softening. For fixed $\eta$, time-steps decrease as $\epsilon^{1/2}$ in PKDGRAV and for the EpsAcc criterion of GADGET, but are unchanged as the softening decreases for the other GADGET criteria.

The effects of this are illustrated in Fig. 8, which shows the result of adopting $f\eta \sim 0.2$ whilst gradually reducing the softening to values almost two orders of magnitude below optimal. For RhoS-gAcc[5] (solid triangles), $f\eta = 0.15$ seems appropriate for $\epsilon$ close to or slightly smaller than $\epsilon_{\rm opt} \approx 10\,h^{-1}$ kpc, but an artificially low density core clearly develops for softenings well below the optimal value. This behaviour is not seen in the case of EpsAcc, where convergence appears firm even for values of $\epsilon$ approaching the large angle-deflection limit, $\epsilon_{2b}$.

We emphasize that this does *not* signal a failure of the RhoSgAcc criterion; rather, it implies that the time-steps chosen with $f\eta \sim 0.2$ are not short enough to achieve convergence when $\epsilon \ll \epsilon_{\rm opt}$. Indeed, choosing RhoSgAcc and $f\eta \approx 0.2(\epsilon/\epsilon_{\rm opt})^{1/2}$ for small softenings eliminates the artificially low density core shown in Fig. 8 at a cost in the total number of time-steps, $N_{\rm ftot}/N$, not very different from that required by EpsAcc. This demonstrates clearly the need to take smaller time-steps when $\epsilon \ll \epsilon_{\rm opt}$.

How should time-steps scale with $\epsilon$? Equation (13) suggests a linear dependence when discreteness effects dominate, $\Delta t \propto \epsilon$, although the firm convergence seen for EpsAcc in Fig. 8 indicates that a gentler dependence, $\Delta t \propto \epsilon^{1/2}$, may actually suffice. This is because the actual individual time-steps in this criterion are determined by the ratio, $(\epsilon/a_i)^{1/2}$, and accelerations are high during close encounters when softenings are small. As a result, the 'effective' size of EpsAcc time-steps scales roughly linearly with softening when

---

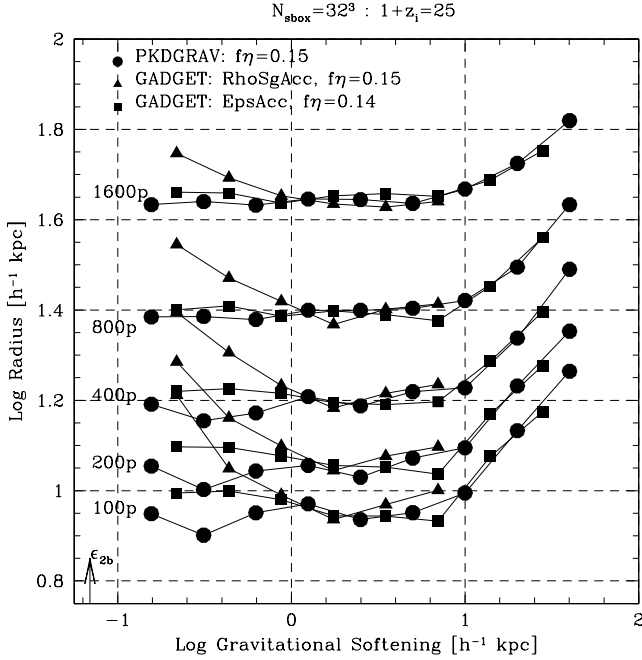[5] For simplicity, here we only discuss RhoSgAcc; similar results apply to VelAcc.

**Figure 8.** Radii enclosing various mass fractions measured at $z = 0$ in our $32^3$ simulations as a function of the gravitational softening scalelength, $\epsilon$. Pairwise interactions become Newtonian at distances exceeding $2\epsilon$. The virial radius of the halo is $r_{200} = 205\,h^{-1}$ kpc and the total number of particles within this radius is $N(r_{200}) \approx 6200$. Note that for PKDGRAV and EpsAcc runs the mass profile is independent of softening for $\epsilon < 6\,h^{-1}$ kpc, provided that the softening remains larger than $\epsilon_{2b}$, the minimum needed to prevent large-angle deflections during particle collisions (Section 3.1). For RhoSgAcc, the choice $f\eta = 0.15$ leads to convergence for $\epsilon > 1\,h^{-1}$ kpc, but results in large deviations for smaller softenings. See Section 4.2 for details. This figure is in colour on *Synergy*, the online version of the journal.

$\epsilon \ll \epsilon_{opt}$. We have verified this by comparing the 'maximum' number of time-steps, defined by the total number of time-steps taken by a hypothetical particle which, at all times, has the minimum time-step of all particles in the system, with the minimum number of *constant* time-steps required for convergence (see Section 3.2). The agreement is quite good.

### 4.3 Adaptive versus constant time-step

Finally, we investigate the computational gain/loss associated with adopting a constant or adaptive time stepping technique when a criterion such as EpsAcc is selected. Again, we assume that the bulk of the computational work is invested in computing individual accelerations, although this measure neglects the cost of tree construction. Ordinarily, tree-making contributes a small fraction of the CPU budget, but this is not necessarily the case in multiple time-stepping schemes when a full tree structure is recalculated every time particles in the smallest time bin are advanced. This is the case in the version of PKDGRAV that we tested. GADGET, on the other hand, recomputes trees only after a certain number of interactions have been computed (Section 2.1), so the comparison is not straightforward.

We have chosen for the comparison maximally converged PKDGRAV runs, i.e. those requiring the minimum number of time-steps for full convergence. The main conclusion may be gleaned from Table 2, where we list the total number of force computations, $N_{ftot}$, for runs

**Table 2.** Properties of maximally converged runs (PKDGRAV).

| $N_{sbox}$ | $\epsilon$ ($h^{-1}$ kpc) | $N_{\Delta t}$ (constant) | $N_{ftot}$ (constant) | $\bar{N}_{\Delta t}$ (multiple) | $N_{ftot}$ (multiple) |
|---|---|---|---|---|---|
| $32^3$ | 10.0 | 800 | $2.6 \times 10^7$ | 640 | $2.1 \times 10^7$ |
| | 2.5 | 1600 | $5.2 \times 10^7$ | 1342 | $4.4 \times 10^7$ |
| | 0.625 | 25600 | $8.4 \times 10^8$ | 2777 | $9.1 \times 10^7$ |
| $64^3$ | 2.5 | 3200 | $8.4 \times 10^8$ | 1754 | $4.6 \times 10^8$ |
| $128^3$ | 1.25 | 3200 | $6.7 \times 10^9$ | 2956 | $6.2 \times 10^9$ |

with $32^3$ high-resolution particles[6] and three different choices for the gravitational softening; $\epsilon = 10\,h^{-1}$ kpc ($\approx \epsilon_{opt}$), as well as $\epsilon = 2.5$ and $0.625\,h^{-1}$ kpc. The number of constant time-steps needed for full convergence depends sensitively on softening, as discussed in Section 3; $N_{\Delta t}$ climbs from 800 to 25 600 as $\epsilon$ decreases from 10 to $0.625\,h^{-1}$ kpc. The total number of force calculations is directly proportional to $N_{\Delta t}$, and increases from $2.6 \times 10^7$ to $8.4 \times 10^8$.

Table 2 shows that, when adaptive multiple time-steps are allowed, the total number of force calculations needed is comparable when $\epsilon \sim \epsilon_{opt}$, but far fewer when the softening is well below the 'optimal' value. This demonstrates that the small time-steps required when the softening is well below the 'optimal' value are only needed briefly by a small subset of particles undergoing close encounters. Adaptive multi-stepping schemes vastly outperform the fixed time-step approach when $\epsilon \ll \epsilon_{opt}$.

### 4.4 Summary

To summarize, we find that all time-stepping criteria we have considered can deliver convergence at comparable cost. However, the EpsAcc criterion is the one that suffers least from overheads related to computing values for individual time-steps, and thus appears to be the most efficient of the criteria explored in this study. We emphasize, however, that this choice is primarily empirical; further investigation may very well lead to better and more efficient alternatives than any of those considered here.

Furthermore, for softenings close to the 'optimal' value, the computational gain that results from adopting multi-stepping schemes is rather modest, especially considering that the implementation of multi-stepping incurs a non-negligible cost in terms of memory usage and bookkeeping. Smaller softenings increase the importance of discreteness effects and lead to integrations with very small time-steps dictated by occasional encounters. Multi-stepping schemes are strongly favoured under these circumstances.

### 5 THE ROLE OF OTHER NUMERICAL PARAMETERS

Proper convergence requires, of course, that appropriate choices be made for *all* relevant parameters. We now turn to the analysis of the separate role of other numerical parameters. Unless explicitly stated, we undertake the analysis of each parameter using only runs for which all other parameters take 'converged' values. This can only be done after a large parameter space search because the effects of combinations of some parameters may be subtle. For example, a time-step that is adequate for some gravitational softening may be

---

[6] For ease of comparison, we have not reduced in this series the number of high-resolution particles through the 'amoeba' procedure described in the Appendix for runs listed in this Table 2.

inadequate when the softening is substantially modified. Because of this restriction, the results in the following subsections contain, for clarity, only a small fraction of all runs performed.

### 5.1 The gravitational softening

Large cosmological simulations generally use a single particle mass and thus resolve systems of different mass with different numbers of particles. This implies that it is possible to choose 'optimal' values of the softening only for a small range of halo masses, because $\epsilon_{\rm opt} \propto r_{200}/N_{200}^{1/2} \propto N_{200}^{-1/6}$. This may not be too restrictive for the resimulations we discuss here, because they focus on one system at a time, but it does affect significantly large cosmological simulations. If, for example, an optimal softening choice is made for the most massive system expected to form at, say, $z = 0$, it will be smaller than the optimal value for less massive systems present at the same time [see equation (15)]. How are their mass profiles affected and what regions in such systems may be considered converged?

To address this question, we have undertaken a large series of simulations where the softening, $\epsilon$, was varied systematically while choosing 'converged' values of all other parameters. We have explicitly checked that, for example, doubling or halving the number of time-steps (or the initial redshift) has no appreciable effect and that, for a given number of particles, the results discussed in this subsection depend only on $\epsilon$.

We show the results of this series in Fig. 8, where radii enclosing various mass fractions are shown as a function of $\epsilon$ in simulations with $32^3$ high-resolution particles. Because $r_{200} \approx 205\,h^{-1}$ kpc, the radii shown in Fig. 8 probe a large fraction of the halo's radial extent, between 4 per cent and 22 per cent of the virial radius. For this system, $\epsilon_{2b} = 0.066\,h^{-1}$ kpc $\approx 3.2 \times 10^{-4}r_{200}$ and $\epsilon_{\rm opt} \sim 10\,h^{-1}$ kpc $\approx 4.9 \times 10^{-2}r_{200}$.

As Fig. 8 shows, the mass profiles obtained with the two codes agree to better than 20 per cent (i.e. to better than 10 per cent in circular velocity) even for radii containing as few as 100 particles. Full convergence is achieved for a wide range of softening scales, provided that $\epsilon_{2b} < \epsilon \lesssim 6\,h^{-1}$ kpc. The mass profiles are essentially unchanged even as the softening is varied by almost two orders of magnitude.

A second important point to note in Fig. 8 is that for $\epsilon \sim 12\,h^{-1}$ kpc (only slightly larger than $\epsilon_{\rm opt}$) the profile deviates from the converged one even as far out as $60\,h^{-1}$ kpc; i.e. more than five times the softening length. This contrasts with the results for $\epsilon \sim 6\,h^{-1}$ kpc, where the mass profile appears to have converged down to almost one softening length scale. Clearly, the assumption that mass profiles are affected out to a certain multiple of the softening length is an oversimplification that is *not* supported by these results.

What determines the smallest converged radius for a given softening length scale? Because softenings introduce a characteristic acceleration on small scales, it is instructive to consider the mean acceleration that particles experience as a function of the distance from the centre of the system. This radial acceleration profile, $a(r) = GM(r)/r^2 = V_c^2(r)/r$, is shown in Fig. 9 for two series of runs where the gravitational softening has been varied systematically by two orders of magnitude. The values of the softening in each run are shown with small vertical arrows near the bottom of the figure. Solid and dashed curves correspond to runs with $64^3$ and $32^3$ particles in the high-resolution box, respectively. As the softening is decreased from $\epsilon \sim 0.1r_{200}$ by successive factors of 2, the acceleration profiles become steeper and converge to a unique profile for $\epsilon \lesssim 0.03r_{200} \approx 6\,h^{-1}$ kpc, as shown in Fig. 9. The convergent profile
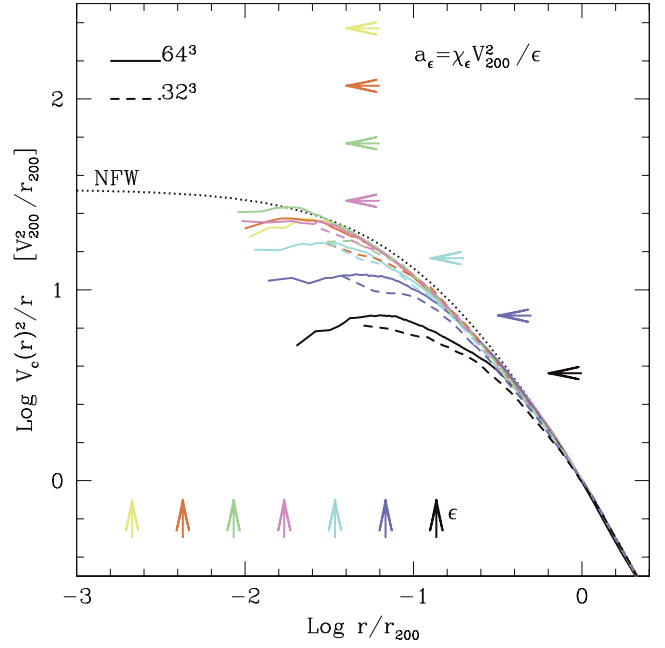


**Figure 9.** Spherically averaged 'acceleration' profiles ($V_c^2(r)/r$) for $64^3$ and $32^3$ runs, shown for several choices of the softening scalelength, $\epsilon$. The dotted curve corresponds to the acceleration profile of an NFW model with concentration $c = 10$. The vertical arrows denote the value of the softening parameter, $\epsilon$, for each run. The profiles line up, from bottom to top, in order of decreasing $\epsilon$. As $\epsilon$ approaches $\sim 0.01r_{200}$, the acceleration profiles converge to a solution similar to the fiducial NFW curve. Profiles significantly affected by the softening deviate from the converged result at a radius where the acceleration matches the characteristic acceleration associated with the circular velocity of the halo, $V_{200}$, and $\epsilon$: $a_\epsilon = \chi_\epsilon V_{200}^2/\epsilon$, with $\chi_\epsilon \approx 0.5$. The values of $a_\epsilon$ corresponding to each adopted value of $\epsilon$ are shown by the horizontal arrows.

is well approximated by an NFW profile with $c = 10$, shown by a dotted curve in Fig. 9.

We note two interesting features of the acceleration profiles shown in Fig. 9. The first is that the effects of softening on the acceleration profile depend rather weakly on the number of particles used; for given $\epsilon$, the profiles corresponding to runs with $32^3$ and $64^3$ particles agree reasonably well, and they approach the same 'converged' profile for $\epsilon \lesssim 0.03r_{200}$. The second feature is that acceleration profiles deviate from the 'converged' profile near the centre for larger values of the softening. Interestingly, deviations occur at radii where the acceleration exceeds a 'characteristic' acceleration,

$$a_\epsilon = \chi_\epsilon V_{200}^2/\epsilon, \tag{17}$$

which depends only on the circular velocity of the halo and on the value of the softening adopted. This characteristic acceleration is shown (for $\chi_\epsilon \approx 0.5$) with horizontal arrows in Fig. 9. The mass profile of a simulated halo becomes unreliable for accelerations exceeding $a_\epsilon$.

This result suggests an empirical interpretation of the effects of softening on the mass profile of a simulated halo; the choice of gravitational softening imposes an effective limit on the accelerations that may be adequately reproduced in the system. This is interesting because, for systems with density profiles similar to that proposed by NFW, there is a *maximum* acceleration that particles may experience. Indeed, $a(r) = V_c^2/r$ tends to a well-defined maximum

$$a_{\rm max} = \frac{c^2/2}{\ln(1+c) - c/(1+c)} \frac{V_{200}^2}{r_{200}} \tag{18}$$

as $r$ approaches zero. If $\epsilon$ is such that

$$a_\epsilon \gtrsim a_{max}, \qquad (19)$$

then it appears to impose no substantial restriction on the mass profile. For example, Fig. 6 shows that the converged mass within $\sim 1\,h^{-1}$ kpc appears not to change as $\epsilon$ varies between 1.25 and $3.5\,h^{-1}$ kpc. At face value, this would appear to imply that the mass profile can be trusted down to almost one third of the softening length scale when the condition expressed in equation (19) is satisfied. In order to be conservative, however, we hereafter assume that converged radii cannot be less than $\epsilon$.

How does the upper limit on $\epsilon$ dictated by this constraint compare with $\epsilon_{opt}$, the minimum needed to prevent discreteness effects and to minimize the number of time-steps? The answer depends on the number of particles, as well as on the concentration of the system, and imposes an effective lower limit on the number of particles needed to satisfy both conditions simultaneously, $N_{200} \gtrsim (2c)^4/(\ln(1+c) - c/(1+c))^2$. For $c \approx 10$, we find that roughly 70 000 particles within the virial radius are needed to carry out a simulation where the softening is small enough not to restrict significantly the resolution of the inner mass profile and is large enough to prevent discreteness effects from hindering the computational efficiency of the calculation.

To summarize, provided that all other numerical parameters are chosen appropriately, the effect of the softening on the spherically averaged mass profile is to impose a maximum acceleration scale above which results cannot be trusted. The mass profile of a simulated halo converges at radii where the mean acceleration does not exceed a characteristic value imposed by the softening, $a(r) = V_c^2(r)/r \lesssim a_\epsilon = \chi_\epsilon V_{200}^2/\epsilon$, where $\chi_\epsilon$ is empirically found to be $\sim 0.5$ if $\epsilon$ is expressed as a spline-softening scalelength.

## 5.2 The initial redshift

The starting redshift, $z_i$, determines the overall initial amplitude of density fluctuations in the simulation box. If $z_i$ is too low, small scales may already be in the non-linear regime, invalidating the assumptions of the procedure outlined in Section 2.2. Initial redshifts cannot be chosen to be too high either, because the more uniform the periodic box, the more difficult the task of evaluating accurate forces in treecodes, such as those we employ here, becomes. A compromise must therefore be struck between these competing demands and we derive in this section a simple empirical prescription that ensures convergence in the mass profiles of simulated CDM haloes at $z = 0$.

Fig. 10 shows the radii of various mass fractions (at $z = 0$) as a function of the initial redshift of the simulation. The top and bottom panels refer to the same halo, using two different particle numbers in the high-resolution box: $32^3$ (bottom) and $64^3$ (top). Each curve is labelled by the enclosed number of particles. The inner mass profile of the halo converges as the initial redshift is increased. Convergence to better than 10 per cent at all radii is achieved for $25 < 1 + z_i < 100$, and even for the highest $z_i$ tested there is no clear departure from convergence. We have checked explicitly that this result does not depend on the particular time-stepping choice; a similar series with the SgAcc criterion gives similar results.

The data in Fig. 10 also suggest that convergence may be achieved at lower $z_i$ when $32^3$ particles are used rather than $64^3$. A possible explanation for this is presented in Fig. 11, where we plot, for each radial shell, the deviations from the converged value as a function of the (theoretical) rms mass fluctuation on the smallest resolved mass scale at $z_i$, $\sigma(m_p, z_i)$ ($m_p$ is the mass of one high-resolution particle). In terms of this variable, the $32^3$ and $64^3$ results are indis-
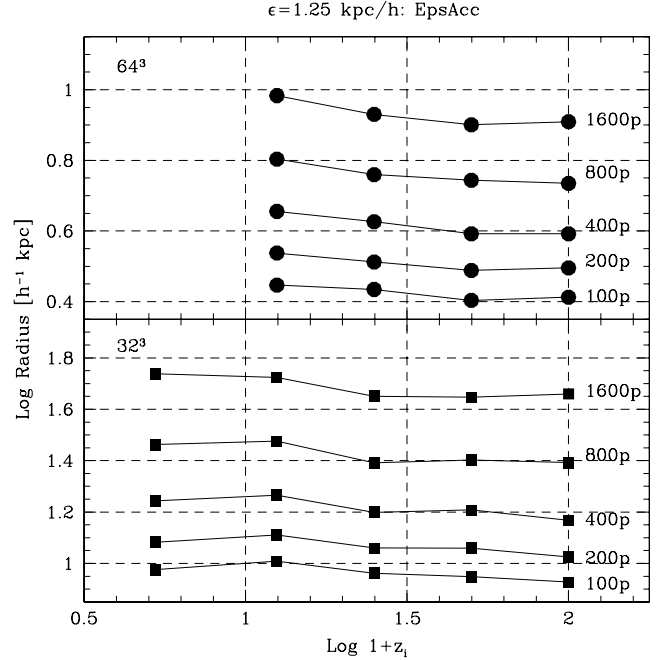


$\epsilon = 1.25$ kpc/h: EpsAcc

**Figure 10.** As Fig. 8, but as a function of the initial redshift of the simulation. Convergence is seen for $z_i \gtrsim 25$ in the $32^3$ runs and for $z_i \gtrsim 49$ in the $64^3$ runs. Starting at lower initial redshifts causes halo mass profiles to develop an artificially low density core. This figure is in colour on *Synergy*, the online version of the journal.

tinguishable, showing convergence down to the 100-particle mass shell when $z_i$ is chosen so that $\sigma(m_p, z_i) \lesssim 0.3$. This is a simple empirical rule for choosing the starting redshift, which we adopt hereafter.

One advantage of this rule is that, for power spectra such as CDM, $\sigma(m_p)$ is only weakly dependent on mass on small scales, so the initial redshift can be chosen almost independently of the number of particles. For example, even for the highest number of particles considered in our study ($N_{sbox} = 256^3$, $m_p = 6.5 \times 10^5\,h^{-1}$ M$_\odot$) the starting redshift condition is satisfied for $1 + z_i \gtrsim 42$, so that $1 + z_i = 50$ can be safely used for all of our simulations, regardless of $N$.

## 5.3 Force accuracy

Accurate forces are an obvious requirement for numerical convergence, and we investigate here the role of force accuracy parameters in the mass structure of dark haloes. This is important as treecodes are based on approximate multipole expansion-based methods that are vulnerable to inaccuracies in the force calculations. Although accuracy can always be improved by adopting, for example, stricter node-opening criteria, this comes usually at the cost of substantial loss in computational efficiency. It is therefore important to determine what is the minimum force accuracy needed to achieve convergence in order to maximize the efficiency of the simulation.

Force accuracy is controlled in GADGET (in the configuration used in this study, see Section 2.1.1) through two main parameters: a compile-time flag, –DBMAX, which, if enabled, restricts node opening to a list of cells *guaranteed* not to contain the particle under consideration; and the parameter $f_{acc}$ (called ErrTolForceAcc in GADGET's parameter file), which controls dynamically the updating of the tree-node-opening criterion (Springel et al. 2001). Fig. 12 shows
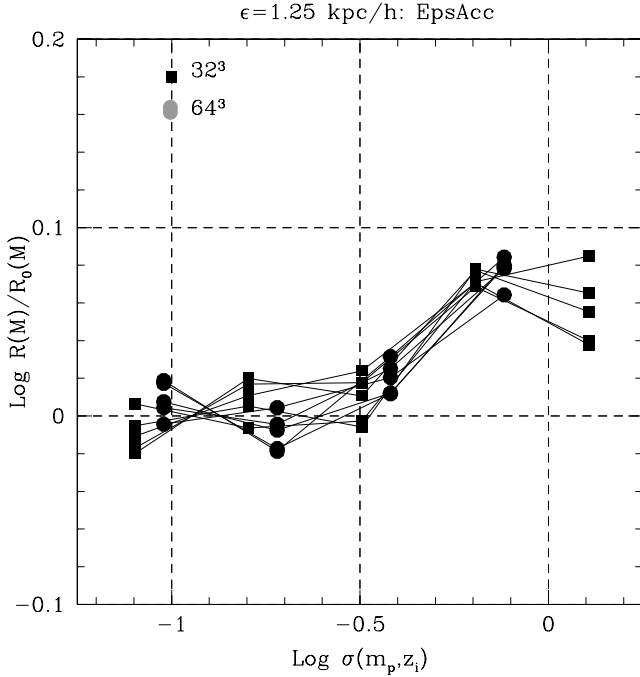
$\epsilon = 1.25$ kpc/h: EpsAcc

**Figure 11.** The radii of various mass shells, as in Fig. 10, but normalized to the 'converged' value of the radius for each shell as a function of $\sigma(m_p, z_i)$, the linear rms fluctuation on the scale of the particle mass at $z = z_i$. Note that convergence is achieved at all radii when $\sigma(m_p, z_i) \lesssim 0.3$. This figure is in colour on *Synergy*, the online version of the journal.

the radii of various mass shells in our standard halo as a function of $f_{acc}$. The solid squares show the results obtained without setting the –DBMAX option in GADGET. Convergence is achieved in this case for quite small values of the accuracy parameter, $f_{acc} \lesssim 0.003$. The reason behind the slow convergence seen in Fig. 12 appears to be related to rare but substantial errors incurred in GADGET's tree-walking procedure when the boundaries of open nodes are *not guaranteed* to exclude the particle under consideration (Salmon & Warren 1993). Disallowing this possibility (i.e. enabling –DBMAX during compilation) leads to much improved convergence relative to the parameter $f_{acc}$, as can be seen from the solid circles in Fig. 12. There is almost no systematic trend with $f_{acc}$ when –DBMAX is enabled, even for $f_{acc} \approx 1$.

The main effect of enabling –DBMAX is to suppress a tail of large errors that, although rare, appear to have a significant effect on the final mass profile. This can be seen in Fig. 13 where we show the cumulative distribution of errors in accelerations computed on a $z = 0$ snapshot of a simulation with $32^3$ high-resolution particles. Force errors were measured by comparing with the result obtained by direct summation. Solid and dashed curves give the result of opening nodes with the 'relative' opening criterion proposed by Springel et al. (2001), with and without the –DBMAX option, respectively. In each case, results are shown for tolerance parameters $f_{acc} = 0.001$, 0.003 and 0.01 (from left to right). We also show results for the traditional Barnes–Hut opening criterion (dotted curves), with opening angles $\theta = 0.5$, 0.75 and 1.0 (from left to right).

We have chosen a rather small value of the softening in Fig. 13 to emphasize graphically the point that a long tail of errors may exist when the –DBMAX option is not enabled; note, for example, that errors of up to 100 per cent or larger are present in this case when $f_{acc} = 0.01$ (rightmost dashed curve). Such errors are not present when –DBMAX is on (solid curves).



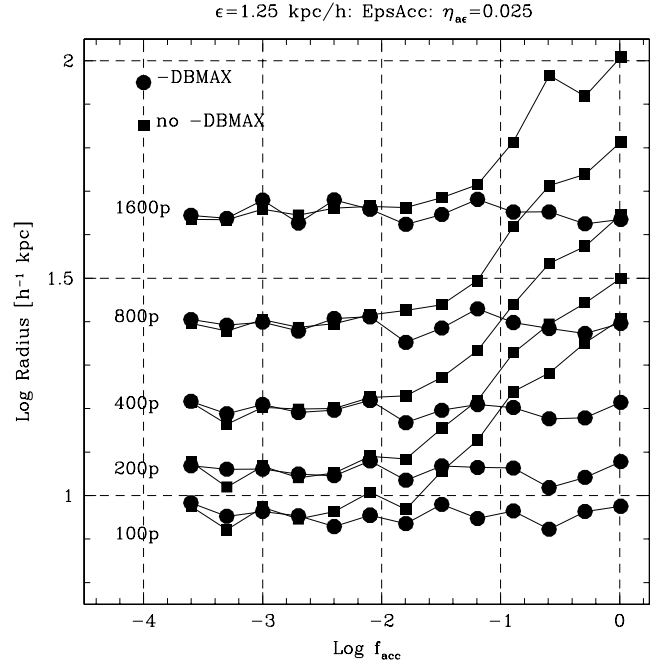$\epsilon = 1.25$ kpc/h: EpsAcc: $\eta_{a\epsilon} = 0.025$

**Figure 12.** As Fig. 8, but for radii as a function of the GADGET force accuracy parameter, $f_{acc}$ (ErrTolForceAcc in GADGET's parameter file). The solid squares show results without enabling the extra-accuracy flag –DBMAX during compilation. The solid circles show results enabling –DBMAX. When this flag is on, the effects of $f_{acc}$ on the mass are mild, and good convergence is achieved even for rather large values of $f_{acc}$. When –DBMAX is off, $f_{acc} \lesssim 10^{-3}$ is needed to ensure convergence. This figure is in colour on *Synergy*, the online version of the journal.

The inset compares the accuracy obtained for all of these choices as a function of the invested computational cost. 'Accuracy' is here taken as the 98 per cent percentile force error, and the computational cost is measured in terms of the average number of node–particle interactions per force evaluation. For a given accuracy, the Barnes–Hut criterion results in higher cost than the criterion adopted in GADGET.

We conclude that enabling –DBMAX and adopting $f_{acc} \lesssim 0.01$ is sufficient to study the inner structure of dark matter haloes. Alternatively, adopting a redshift-dependent Barnes–Hut node-opening criterion, such as in PKDGRAV, where $\theta = 0.55$ is used for $z > 2$ and $\theta = 0.7$ for $z < 2$, seems also to give adequate results.

### 5.4 The number of particles

The total number of particles is a critical parameter to choose when running a cosmological $N$-body simulation. Because the computation time will scale at best linearly with $N$, we must try and use as few particles as possible to achieve the goals of the programme. As mentioned in Section 1, our main goal is to provide robust and accurate measurements of the circular velocity (or mass) profile of dark matter haloes down to about the inner *1* per cent of the virial radius. This corresponds to $\sim 2.2\,h^{-1}$ kpc in the case of the Milky Way if its halo has the same circular velocity as the disc. This is clearly the minimum resolution required for meaningful comparison with observed rotation curves.

In the preceding discussion, we have determined the optimal choice of softening, time-stepping, force accuracy and starting redshift required to obtain repeatable and robust measurements of the
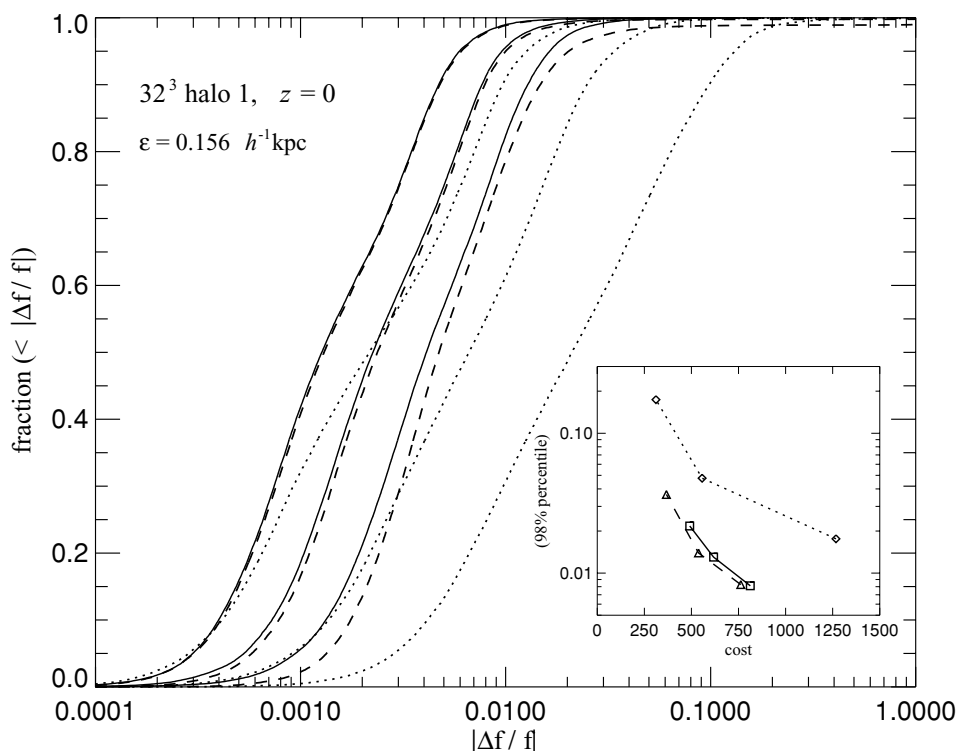
**Figure 13.** Cumulative error distributions of GADGET's force computation for various choices of opening criterion and tolerance parameter. We used the particle distribution of the $z = 0$ snapshot of a run with $32^3$ high-resolution particles and measured force errors by comparing with the result obtained by direct summation. Solid and dashed curves give the result of opening nodes with the 'relative' opening criterion proposed by Springel et al. (2001), with and without the –DBMAX option, respectively. Results are shown for tolerance parameters $f_{acc} = 0.001$, 0.003 and 0.01 (from left to right). The dotted curves show results for the traditional Barnes–Hut opening criterion, with opening angles $\theta = 0.5$, 0.75 and 1.0 (from left to right). The inset compares the accuracy obtained for all of these choices as a function of computational cost. See the text for more details.

circular velocity profile of a simulated CDM halo down to radii containing as few as 100 particles. Repeatability and robustness relative to these parameters are, of course, necessary conditions for convergence, but we must still demonstrate that the results do not depend on the total number of particles chosen.

How many particles must a region contain so that the circular velocity (or, equivalently, the mean inner density) converges? We use the lessons from the preceding subsections to explore the dependence of the mass profile of simulated dark haloes on the number of particles used. We consider only runs which meet the requirements discussed previously, so that, for each choice of $N$, we only present 'converged' results relative to other parameters. Our tests span an unprecedented range of 512 in particle number, from $32^3$ to $256^3$ particles in the high-resolution simulation cubes.

Our main results are summarized in Fig. 14, where we show, as a function of the enclosed number of particles, the mean inner density contrast measured at various radii from the centre of the halo. In this figure, for example, solid triangles show the mean inner density contrast measured at ∼20 per cent of the virial radius. From left to right, each group of solid triangles indicates the results of runs with $32^3$, $64^3$, $128^3$ and $256^3$ particles in the high-resolution cube. These runs have 6200, 49 600, 397 000, and $3.2 \times 10^6$ particles within $r_{200}$, respectively. As the number of particles increases, fewer runs are shown, because of the increasing computational cost. At the highest resolution, with $256^3$ particles in the high-resolution cube, we have completed only one simulation. This run is comparable to the highest-resolution simulations reported in the literature so far.

Fig. 14 shows a number of important trends. Consider, for example, the radius corresponding to *2* per cent of $r_{200}$ (solid circles). In the $32^3$ runs, this radius contains 1.6 per cent of the halo mass (∼100 particles). The mass within this radius is seen to increase significantly as the number of particles increases; the density contrast climbs from ∼$1.2 \times 10^5$ (in the $32^3$ runs) to ∼$2.5 \times 10^5$ (in the $64^3$ runs) before stabilizing at ∼$3 \times 10^5$ when $N_{sbox}$ reaches $128^3$ and $256^3$. Clearly, 100 particles are *not enough* to trace reliably the mass profile of a simulated halo, in disagreement with the conclusions of Klypin et al. (2001), who argue that 100–200 particles suffice to resolve the inner mass profile when other parameters are chosen properly.

The situation is different for the 1000-particle radius in the $32^3$ runs, which correspond to about 10 per cent of the virial radius. The density contrast within this radius is ∼$2.5 \times 10^4$, and remains essentially unchanged as the number of particles increases by a factor of 512. The data presented in Fig. 14 thus support the conclusions of Moore et al. (1998); resolving regions closer to the centre, where the density contrast is higher, demands increasingly large particle numbers. Although 300 particles in the $32^3$ runs are almost enough to resolve the 6 per cent radius, they fall well short of what is needed to resolve the much higher overdensity characteristic of the 1 per cent radius.

How many particles are needed to resolve a given radius? Moore et al. (1998) propose that converged regions are delineated by (one-half) the mean interparticle separation within the virial radius, $0.5(4\pi/3N_{200})^{1/3}r_{200}$, whereas Fukushige & Makino (2001) suggest that the innermost resolved radius cannot be smaller than the radius
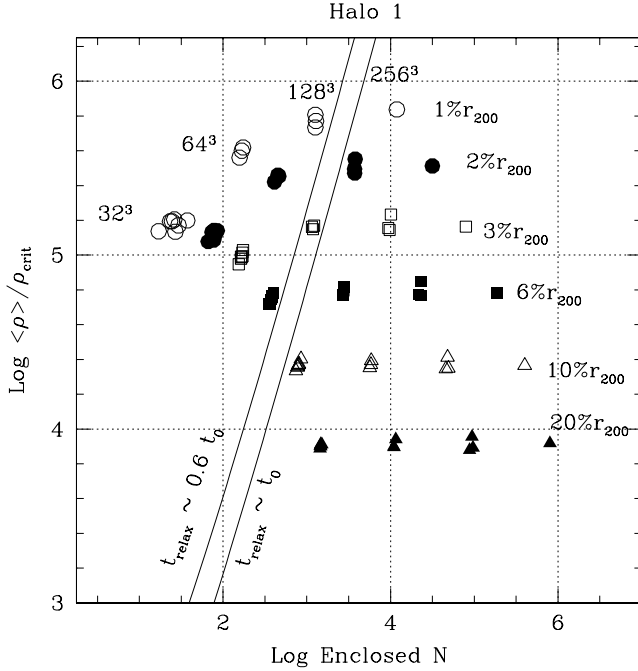
**Figure 14.** Mean inner density contrast as a function of the enclosed number of particles in four series of simulations varying the number of particles in the high-resolution box, from $32^3$ to $256^3$. Each symbol type corresponds to a fixed fraction of the virial radius, as shown by the labels on the right. The number of particles needed to obtain robust results increases with density contrast, roughly as prescribed by the requirement that the collisional relaxation time-scale should remain longer than the age of the Universe. According to this, robust numerical estimates of the mass profile of a halo are only possible to the right of the curve labelled $t_{\rm relax} \sim 0.6t_0$. This figure is in colour on *Synergy*, the online version of the journal.



**Figure 15.** Circular velocity profiles of 'converged' runs with different numbers of high-resolution particles. Profiles are only plotted for radii where the convergence criteria derived in this paper are satisfied. Several curves are shown for the cases of $32^3$, $64^3$ and $128^3$ particles, corresponding to runs where all other numerical parameters take converged values. For clarity, a small selection of runs have been chosen; those with softenings are indicated by the small vertical arrows. The convergent profile that emerges for this halo is roughly independent of the number of particles and resembles closely the model proposed by NFW, with $c = 10$. For this halo, steeply cusped density profiles are not favoured. The profiles labelled 'Moore et al.' and 'NFW' have been matched at the peak of the circular velocity profile.

where the two-body relaxation time becomes shorter than the age of the Universe.

Our results appear to favour the latter interpretation. For example, the criterion of Moore et al. would predict that the $32^3$ runs could be trusted down to 4.5 per cent of the virial radius, but it is clear from Fig. 14 that convergence in this case is achieved only for radii beyond 6 per cent of $r_{200}$. On the other hand, all simulations can be seen to converge at radii larger than the radius where the average collisional relaxation time roughly matches the age of the Universe. This is shown by the (almost vertical) line labelled $t_{\rm relax} \sim t_0$, where we define

$$\frac{t_{\rm relax}(r)}{t_{\rm circ}(r_{200})} = \frac{N}{8\ln N} \frac{r/V_{\rm c}}{r_{200}/V_{200}} = \frac{\sqrt{200}}{8} \frac{N}{\ln N} \left(\frac{\bar{\rho}}{\rho_{\rm crit}}\right)^{-1/2}. \quad (20)$$

$t_{\rm circ}(r_{200}) \sim t_0$, and $N = N(r)$ is the enclosed number of particles. For reference, the curve on the left indicates $t_{\rm relax} = 0.6 t_{\rm circ}(r_{200}) \sim 0.6 t_0$. As shown in Fig. 14, the density profile converges at radii that enclose enough particles so that $t_{\rm relax}(r) \gtrsim 0.6 t_0$.

We emphasize that this criterion is mainly empirical, and does not necessarily imply that particles in regions where the relaxation time is shorter than $\sim 0.6 t_0$ actually evacuate the central regions as a result of two-body encounters. Indeed, we would expect the inner mass profile to evolve as a result of collisions on the much longer 'evaporation' time-scale, $t_{\rm evap} \approx 136 t_{\rm relax}$ (Binney & Tremaine 1987), a proposition that finds support in simulations of the evolution of isolated equilibrium *N*-body systems (Hayashi et al. 2002). In ad-
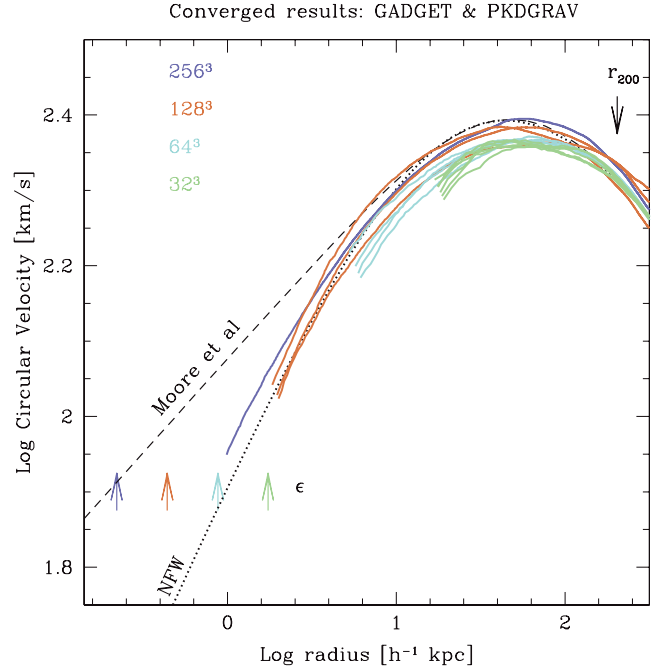
dition, the heating rate near the centre is likely to be dominated by the presence of substructure rather than by particle–particle collisions, complicating the interpretation. Our result is thus reminiscent of the work of Weinberg (1998), who emphasizes the difficulty of achieving the collisionless limit in *N*-body systems and the possibility that fluctuation noise may lead to relaxation effects important on all scales.

Despite this difficulty, it seems clear from Fig. 14 that resolving density contrasts exceeding $10^6$ requires $\gtrsim 3000$ particles within that radius, or over 3 million particles within the virial radius. Providing robust numerical predictions of the mass structure of CDM haloes on scales that can be compared directly with observations of individual galaxies is thus a very onerous computational task.

### 5.5 Optimal parameters – a worked example

The many considerations discussed in the previous sections make the selection of optimal parameters for any given *N*-body run a delicate and complicated business. It may be helpful to go through how one might choose optimal parameters for a specific calculation, for example a simulation like the largest one ($N_{\rm sbox} = 256^3$) we consider in this paper. This run has $\sim 3 \times 10^6$ particles within the virial radius at $z = 0$, and is the largest we can easily carry out with resources currently available to us. Fig. 14 and the discussion in Section 5.4 suggest that this number of particles should be sufficient to obtain converged results down to about $r_{\rm conv} = 0.005 r_{200}$. Equation (15) suggests that a softening parameter $\epsilon = 0.0025 r_{200}$ will be near

optimal for obtaining an efficient integration almost unaffected by discreteness effects. As Fig. 9 demonstrates, this softening is small enough relative to our target $r_{conv}$ that it should not compromise the radial structure. For these parameters, equation (16) and Fig. 4 then show that a single-time-step integrator should be able to converge in about 5000 equal steps, although we note that this depends on the detailed inner structure of the halo, which is what we are trying to measure. In practice, a series of runs, where the number of particles is gradually increased, is desirable to fine-tune the choice of time-step. Alternatively, the discussion of Section 4 implies that for our preferred multi-time-step integrator (EpsAcc) $\eta = 0.15$ should be small enough to ensure convergence. The discussion of Section 5.2 shows that it should be safe to start the integration at $z_i = 49$.

# 6 THE CIRCULAR VELOCITY PROFILE OF A ΛCDM HALO

Finally, we use the convergence lessons derived above to analyse briefly the inner circular velocity profile of the ΛCDM halo considered here. The results of 'converged' runs are shown in Fig. 15. Each profile is shown only for radii considered converged according to the criteria discussed above. Plotted this way, all profiles, independent of the number of particles, seem to agree to within ∼10 per cent at all radii. The circular velocity increases from the virial radius inwards, reaches a maximum and then drops gradually towards the centre, following closely the dotted curve that represents an NFW profile with concentration $c = 10$. This value of the concentration agrees reasonably well with the results of NFW and of Eke, Navarro & Steinmetz (2001), who find $c \approx 8$–9 for a halo of this mass. Near the centre, the profile is seen to deviate significantly from the steeply cusped profile approaching a central slope of $\beta = 1.5$ proposed by Moore et al. (1998), and agrees better with shallower central slopes such as that of the NFW model.

We emphasize that there is little evidence for convergence to a power-law density profile near the centre, and that the profile continues to become shallower down to the innermost point that our procedure deems converged. Can our results be used to place meaningful constraints on the asymptotic inner slope? At $r_{min} \sim 1\,h^{-1}$ kpc, the smallest radius resolved in our highest-resolution run ($N_{sbox} = 256^3$), both the local and cumulative density profiles are robustly determined:[7] $\rho(r_{min})/\rho_{crit} = 9.4 \times 10^5$ and $\bar{\rho}(r_{min})/\rho_{crit} \approx 1.6 \times 10^6$. These values can be combined with the requirement of mass conservation to place an upper limit to the inner asymptotic slope of the density profile, $\beta < 3(1 - \rho(r_{min})/\bar{\rho}(r_{min})) = 1.2$. In other words, there is not enough mass within $r_{min}$ to support a power-law density profile with a slope steeper than $\beta = 1.2$. We note that this conclusion depends sensitively on our ability to resolve the innermost $1\,h^{-1}$ kpc. If $r_{min}$ were just two or three times larger, the same exercise would not be able to rule out slopes as steep as $\beta = 1.5$.

In summary, our results argue strongly against the very steep central cusps advocated by Moore et al. (1998); Moore et al. (1999), Ghigna et al. (1998); Ghigna et al. (2000) and Fukushige & Makino (1997); Fukushige & Makino (2001). We are in the process of augmenting our sample of haloes in order to firm up this conclusion, so we will defer a detailed analysis of this issue to a later paper in this series.

---

[7] Convergence in the local density actually extends to radii smaller than the minimum converged radius for the more stringent cumulative density.

# 7 CONCLUSIONS

We have performed a comprehensive series of convergence tests designed to study the effect of numerical parameters on the structure of simulated CDM haloes. Our tests explore the influence of the gravitational softening, the time-stepping algorithm, the starting redshift, the accuracy of force computations, and the number of particles on the spherically averaged mass profile of a galaxy-sized halo in the ΛCDM cosmogony. We derive, for each of these parameters, empirical rules that optimize their choice or, when those choices are dictated by computational limitations, we offer simple prescriptions to assess the effective convergence of the mass profile of a simulated halo. Our main results can be summarized as follows:

(i) *Time-step and discreteness effects.* The number of time-steps required to achieve convergence depends primarily on the orbital time-scale of the region to be resolved, but may also be sensitive to the number of particles and the gravitational softening, unless these parameters are chosen so that discreteness effects are unimportant. This requires the gravitational softening to be large enough so that the maximum acceleration during two-body encounters does not exceed the minimum mean-field acceleration in the halo, $\epsilon \gtrsim \epsilon_{acc} = r_{200}/\sqrt{N_{200}}$. Empirically, we find that $\epsilon \approx \epsilon_{opt} = 4\epsilon_{acc}$ gives good results. When this condition is satisfied, the minimum converged radius, $r_{conv}$, is given by the condition that the circular orbit time-scale should be long compared to the time-step, $t_{circ}(r_{conv}) \approx 15(\Delta t/t_0)^{5/6} t_{circ}(r_{200})$. *Substantially smaller* time-steps are needed if $\epsilon < \epsilon_{opt}$. Dark matter densities at $r < r_{conv}$ may be underestimated or overestimated, depending on the integrator and time-stepping schemes used. For example, constant-time-step GADGET runs develop artificially dense, 'cuspy' cores in poorly resolved regions, indicating that the approach to convergence is not always monotonic. This emphasizes the importance of comprehensive convergence tests such as those presented here to validate the results of numerical studies of the inner structure of CDM haloes.

(ii) *Fixed time-step versus adaptive multi-stepping.* Of the several adaptive, multiple time-stepping criteria that we have considered, we have found the best results when time-steps are chosen to depend explicitly on the gravitational softening and on the acceleration, $\Delta t_i = \eta_{a\epsilon}\sqrt{\epsilon_i/a_i}$, with $\eta_{a\epsilon} \sim 0.2$. Experiments with time-stepping choices that do not include explicitly the gravitational softening require the value of the corresponding $\eta$ to be reduced as $\epsilon$ is reduced below the optimal value in order to obtain convergence. In terms of computational cost, we find that multi-time-stepping criteria significantly outperform the use of a single time-step for all particles only for softenings well below the optimal value.

(iii) *Gravitational softening.* The choice of gravitational softening is found to impose a maximum acceleration scale above which simulation results cannot be trusted. This acceleration scale appears to depend mainly on the circular velocity of the halo and on the gravitational softening scale, and is given by $a_\epsilon = \chi_\epsilon V_{200}^2/\epsilon$, with $\chi_\epsilon \sim 0.5$. For *a given particle number*, convergence to better than 10 per cent in the mass profile is obtained at radii greater than $\epsilon$ that also contain more than 100 particles and where the acceleration criterion is satisfied: $a(r) = V_c(r)^2/r \lesssim a_\epsilon$.

(iv) *Starting redshift.* The mass profiles of simulated dark haloes converge provided that the initial redshift is chosen so that the theoretical (linear) rms fluctuations on the smallest resolved mass scale, $m_p$ (the mass of one high-resolution particle) is $\sigma(m_p, z_i) \lesssim 0.3$. Because $\sigma(m_p)$ is a weak function of mass on subgalactic mass scales for CDM-like power spectra, this criterion indicates that a modest starting redshift, such as $1 + z_i \approx 50$, is appropriate

for particle masses as low as $m_p \sim 10^5 \, h^{-1} \, M_\odot$ in the $\Lambda$CDM cosmogony.

(v) *Force accuracy.* The mass profiles of simulated CDM haloes are quite sensitive to the accuracy of the force calculations, and convergence requires care in the choice of node-opening criteria in the treecodes used in our study. Poor force accuracy leads to the development of artificially low density cores. In the case of GADGET, for example, we find that even occasional large errors in the forces may lead to noticeable deviations from converged profiles. To avoid this, it is necessary to choose tree-walking parameters that curtail drastically the tail of the most deviant force calculations, however rare. In GADGET this can be achieved by activating the compiler option –DBMAX. Using up to hexadecapole terms in the node potential expansion and setting a redshift-dependent tree-node-opening criterion, as in PKDGRAV, where $\theta = 0.55$ is chosen for $z > 2$ and $\theta = 0.7$ for $z < 2$, seems also to work well.

(vi) *Particle number.* In order to achieve convergence in the mass profile, enough particles must be enclosed so that the average two-body relaxation time-scale within the region is comparable or longer than the age of the Universe. We find empirically that the condition, $t_{\mathrm{relax}}(r) \gtrsim 0.6 t_0$, describes converged regions well. Because $t_{\mathrm{relax}}$ is roughly proportional to the enclosed number of particles times the local dynamical time-scale, resolving regions near the centre, where density contrasts are high and dynamical time-scales are short, requires substantially more particles than resolving regions more distant from the centre. Of the order of 3000 enclosed particles are needed to resolve regions where the density contrast reaches $10^6$. On the other hand, density contrasts of the order of $10^{4.5}$ require only 100 enclosed particles for numerical convergence. Resolving radii of the order of 0.5 per cent of the virial radius in the first case requires of the order of $3 \times 10^6$ particles within the virial radius.

For most simulations, the most stringent convergence criterion is the relaxation time-scale condition on the number of particles. This implies that there is little choice but to strive for the largest possible $N$ when studying the inner regions of dark matter haloes. This limit is dictated by the available computer resources. Choosing the optimal softening for the adopted number of particles then minimizes the number of time-steps needed to achieve convergence down to the radius where $t_{\mathrm{relax}}(r) \gtrsim 0.6 t_0$. The precise number of time-steps cannot be determined ahead of time, as $t_{\mathrm{relax}}(r)$ depends on the detailed structure of the halo, which is what we are trying to measure. This implies that a series of simulations, where the number of particles is increased gradually, is advisable in order to ensure that optimal parameters are chosen for the highest-resolution run intended.

We have applied our convergence criteria to a $\sim 205$ km s$^{-1}$ $\Lambda$CDM halo in order to investigate the behaviour of the inner slope of the density profile. We find that the slope of the spherically averaged density profile, $\beta = -\mathrm{d} \log(\rho)/\mathrm{d} \log(r)$, becomes increasingly shallow inwards, with little sign of approach to an asymptotic value. At the smallest radius that we consider resolved in our highest-resolution ($256^3$) simulation ($r_{\mathrm{min}} \sim 1 \, h^{-1}$ kpc $\approx 0.005 r_{200}$), the local and cumulative density contrasts are robustly determined, $\rho(r_{\mathrm{min}})/\rho_{\mathrm{crit}} = 9.4 \times 10^5$ and $\bar\rho(r_{\mathrm{min}})/\rho_{\mathrm{crit}} \approx 1.6 \times 10^6$. These values can be combined with the requirement of mass conservation to place an upper limit to the inner asymptotic slope of the density profile, $\beta < 3(1 - \rho(r_{\mathrm{min}})/\bar\rho(r_{\mathrm{min}})) = 1.2$, although it is possible that the slope may actually become even shallower near the centre, as suggested recently by Taylor & Navarro (2001).

Our results thus argue against the very steep values for the asymptotic central slope ($\beta \approx 1.5$) claimed recently by Moore et al. (1998, 1999), Ghigna et al. (1998, 2000) and Fukushige & Makino (1997,

2001). The reasons for this disagreement are unclear at this point, because there are substantial differences in the halo mass, numerical techniques and cosmological model adopted, which hinder a direct comparison between our results and theirs. For example, the works of Moore et al. (1998) and Ghigna et al. (2000) differ from ours in mass scale (they simulated a galaxy cluster while we target a galaxy-sized halo) and in cosmology (they adopted an Einstein–de Sitter CDM cosmogony, whereas we adopt the $\Lambda$CDM model).

Finally, the difference between the conclusions from various authors may just reflect the fact that each group applies different criteria to the identification of the regions deemed trustworthy. We note that models with the very steep ($\beta \sim 1.5$) inner slopes, proposed by the Moore et al. group, and with the shallower slopes that we find here are almost indistinguishable if we restrict our analysis to radii $\gtrsim 2$ per cent of the virial radius. Probing radii within the inner *1* per cent of the virial radius seems to be required to shed light on this controversy. Further simulation work with resolution adequate to address this issue in detail is currently underway.

## REFERENCES

Aarseth S. J., 1985, in Multiple Time Scales. Academic Press, New York. Chapter 12, p. 377
Bardeen J. M., Bond J. R., Kaiser N., Szalay A. S., 1986, ApJ, 304, 15
Barnes J., Hut P., 1986, Nat, 324, 446
Bertschinger E., 2001, ApJS, 137, 1
Bertschinger E., Gelb J. M., 1991, Comput. Phys., 5, 164
Binney J., Tremaine S., 1987, Galactic Dynamics. Princeton University Press, Princeton, NJ.
Bond J. R., Cole S., Efstathiou G., Kaiser N., 1991, ApJ, 379, 440
Cole S., Lacey C., 1996, MNRAS, 281, 716
Crone M. M., Evrard A. E., Richstone D. O., 1994, ApJ, 434, 402
Davis M., Efstathiou G., White S. D. M., Frenk C. S., 1985, ApJ, 292, 371
de Blok W. J. G., McGaugh S. S., Bosma A., Rubin V. C., 2001, ApJ, 552L 23
Dubinski J., Carlberg R. G., 1991, ApJ, 378, 496
Efstathiou G., Davis M., White S. D. M., Frenk C. S., 1985, ApJS, 57, 241
Eke V. R., Navarro J. F., Steinmetz M., 2001, ApJ, 554, 114E
Evrard A. E., Summers F. J., Davis M., 1994, ApJ, 422, 11
Fillmore J. A., Goldreich P., 1984, ApJ, 281, 1
Flores R. A., Primack J. R., 1994, ApJ, 427L, 1
Frenk C. S., White S. D. M., Efstathiou G., Davis M., 1985, Nat, 317, 595
Frenk C. S., White S. D. M., Davis M., Efstathiou G., 1988, ApJ, 327, 507
Fukushige T., Makino J., 1997, ApJ, 477L, 9
Fukushige T., Makino J., 2001, ApJ, 557, 533
Ghigna S., Moore B., Governato F., Lake G., Quinn T., Stadel J., 1998, MNRAS, 300, 146
Ghigna S., Moore B., Governato F., Lake G., Quinn T., Stadel J., 2000, ApJ, 544, 616
Gott J. R. III, Weinberg D. H., Melott A. L., 1987, ApJ, 319, 1
Gunn J. E., Gott J. R. III, 1972, ApJ, 176, 1
Hamilton A. J. S., Matthews A., Kumar P., Lu E., 1991, ApJ, 374L, 1

Hayashi E., Navarro J. F., Taylor J. E., Stadel J., Quinn T. R., 2002, ApJ, submitted (astro-ph/0203004)
Hernquist L., Katz N., 1989, ApJS, 70, 419
Hernquist L., Bouchet F. R., Suto Y., 1991, ApJS, 75, 231
Hoffman Y., Shaham J., 1985, ApJ, 297, 16
Huss A., Jain B., Steinmetz M., 1999, ApJ, 517, 64
Jenkins A., Frenk C. S., White S. D. M., Colberg J. M., Cole S., Evrard A. E., Couchman H. M. P., Yoshida N., 2001, MNRAS, 321, 372
Jernigan J. G., Porter D. H., 1989, ApJS, 71, 871
Jing Y. P., 1998, ApJ, 503, L9
Jing Y. P., Suto Y., 2000, ApJ, 529, L69
Katz N., White S. D. M., 1993, ApJ, 412, 455
Klypin A., Kravtsov A. V., Bullock J. S., Primack J. R., 2001, ApJ, 554, 903
Knebe A., Kravtsov A. V., Gottlöber S., Klypin, A. A., 2000, MNRAS, 317, 630
Kravtsov A. V., Klypin A. A., Bullock J. S., Primack J. R., 1998, ApJ, 502, 48
Lacey C., Cole S., 1993, MNRAS, 262, 627
Mo H. J., White S. D. M., 1996, MNRAS, 282, 347
Moore B., 1994, Nat, 370, 629
Moore B., 2001, in Wheeler J. C., Martel H., eds, Proc. AIP Conf. Vol. 586, 20th Texas Symposium. Am. Inst. Phys., New York
Moore B., Governato F., Quinn T., Stadel J., Lake G., 1998, ApJ, 499, L5
Moore B., Quinn T., Governato F., Stadel J., Lake G., 1999, MNRAS, 310, 1147
Navarro J. F., White S. D. M., 1993, MNRAS, 265, 271
Navarro J. F., White S. D. M., 1994, MNRAS, 267, 401
Navarro J. F., Frenk C. S., White S. D. M., 1996, ApJ, 462, 563
Navarro J. F., Frenk C. S., White S. D. M., 1997, ApJ, 490, 493
Peacock J. A., Dodds S. J., 1996, MNRAS, 280, L19
Pen U., 1997, ApJ, 490, L127
Press W. H., Schechter P., 1974, ApJ, 187, 425
Quinn P. J., Salmon J. K., Zurek W. H., 1986, Nat, 322, 329
Salmon J. K., Warren M. S., 1993, J. Comput. Phys., 111, 136
Sellwood J. A., Kosowsky A., 2001, Gas and Galaxy Evolution. ASP Conf. Ser. Vol. 240, Astron. Soc. Pac., San Francisco
Sheth R. K., Tormen G., 1999, MNRAS, 308, 119
Springel V., Yoshida N., White S. D. M., 2001, New Astron., 6, 79
Stadel J., 2001, PhD thesis, University of Washington
Taylor J. E., Navarro J. F., 2001, ApJ, 563, 483
van den Bosch F. C., Swaters R. A., 2001, MNRAS, 325, 1017
Weinberg M. D., 1998, MNRAS, 297, 101
White S. D. M., 1979, MNRAS, 189, 831
White S. D. M., 1994, Formation and Evolution of Galaxies. Les Houches Lectures, preprint (astro-ph/9410043)
White S. D. M., Zaritsky D., 1992, ApJ, 394, 1

## APPENDIX A: THE GENERATION OF COSMOLOGICAL INITIAL CONDITIONS

Periodic boundary conditions are usually adopted in cosmological simulations for reasons of convenience. The assumption of periodicity implies that the simulation volume as a whole has to have precisely the mean density, a requirement that places restrictions on the size of the region and on the redshifts at which a particular simulation may be considered reliable. On the other hand, with periodic boundaries the density field can be expanded as a sum over a discrete set of periodic plane waves. For a simulation volume which is cubic, the Fourier transform of the density field has the form of a cubic grid in Fourier space. The discrete nature of the power spectrum thus makes it easy to set up Gaussian density fields.

The aim of our procedure to generate initial conditions is to provide a particle realization of a Gaussian density field with the chosen power spectrum, $P(k)$, on scales and at redshifts where linear the-

ory is applicable. Our procedure follows closely that described in Efstathiou et al. (1985), where further details may be found. As in Efstathiou et al. (1985), we use the Zel'dovich approximation to perturb particles from a uniform cubic grid,

$$x(t) = q - b(t)\psi(q), \qquad (A1)$$

where $x$ is the comoving Eulerian coordinate of the particle, $q$ is the Lagrangian coordinate denoting the particle's unperturbed position in the grid, $b(t)$ is the linear growth factor, and $\psi$ is a function that describes the spatial structure of the density field. The function $\psi$ can be expressed in terms of the acceleration field at time $t$,

$$\psi(q) = -\frac{F(q, t)}{ma^2(a\ddot{b} + 2\dot{b}\dot{a})}, \qquad (A2)$$

where $F$ is the force field, $a(t)$ is the expansion factor, $m$ is the particle mass, and a dot denotes a time derivative.

In practice, a realization of the desired fluctuation distribution is created in Fourier space, with random phases and normally distributed amplitudes for the real and imaginary components of each mode. We then multiply by an appropriate Green's function, and transform back to obtain the potential on a spatial mesh. This potential is differenced to obtain $F(q, t)$ which, together with equations (A1) and (A2), gives the displacement field required to generate the desired density fluctuations from a uniform distribution.

Once the displacements from the unperturbed positions have been computed, velocities are assigned to the particles assuming that only growing modes are present. The peculiar velocity is then simply proportional to the displacement vector

$$\dot{x} = -\dot{b}\psi(q). \qquad (A3)$$

In cases such as CDM, where there is significant power on all scales, it is important to avoid unrealistically large initial velocities that may result from large amplitude fluctuations on small scales. Thus we assign peculiar velocities only after recalculating the accelerations using the perturbed particle positions and using equation (A2) to re-estimate $\psi(q)$.

We use a cubic grid distribution of particles to represent a uniform density distribution for all simulations reported here, but it is also possible to use a 'glass' for the unperturbed configuration. As discussed by White (1994), this is a better choice for highly aspherical perturbations, and avoids artefacts that arise from the existence of 'preferred' (Cartesian) directions in cubic grids. This is especially important when attempting to simulate very low mass haloes in CDM cosmogonies, because on those scales the mass fluctuation spectrum is nearly 'flat' ($P(k)$ approaches $k^{-3}$) and collapse proceeds almost simultaneously on many different mass scales in a network of sheets and filamentary structures.

## APPENDIX B: MASS REFINEMENT TECHNIQUE

As discussed above, simulations of periodic boxes are only reliable provided that the box is large enough so that perturbations on scales comparable to the box size are still linear by the present time. This sets a minimum size for periodic boxes designed to be run to $z = 0$ in a $\Lambda$CDM universe. For example, in the case considered in this paper (see Section 2.2) the size of the periodic box is $L_{box} = 32.5\,h^{-1}$ Mpc ($M_{box} = 9.533 \times 10^{15}\Omega_0\,h^{-1}\,M_\odot$), and the variance at $z = 0$ is already $\sigma(M_{box}) \approx 0.3$, at the limit of what may be used to obtain a good representation of large-scale structure in this cosmogony. Clearly, boxes smaller than $32.5\,h^{-1}$ Mpc cannot capture the correct statistical properties of the dark matter distribution at $z = 0$.

Our original low-resolution simulation was carried out with $128^3$ particles.

Even if $512^3$ particles were used in such a box (at the limit of what is possible with today's largest supercomputer if many thousands of time-steps are needed) the mass per particle in a $32.5\,h^{-1}$ Mpc box would be $m_p = 7.1 \times 10^7 \Omega_0\,h^{-1}\,M_\odot$, and a galaxy-sized, $10^{12}\,h^{-1}\,M_\odot$ halo would only contain slightly more than 10 000 particles. A dwarf galaxy halo would have fewer than 1000 particles. Clearly, a different technique is required in order to improve the mass and spatial resolution of the calculation while at the same time accounting properly for the effects of large-scale structure.

The technique most widely adopted so far selects a few systems identified from the final configuration of the periodic box and resimulates the whole box, with coarser resolution everywhere except in the selected regions. This technique has been used in a number of cosmological simulations [see, for example, Katz & White (1993), Navarro & White (1994), Evrard, Summers & Davis (1994) and Moore et al. (1998)], and has become common in high-resolution simulation work targeted at individual systems. The price we pay with this procedure is that to build a statistically significant sample of haloes entails running many different simulations and there is always the possibility of introducing biases during the selection procedure. Having identified a halo in the periodic box for resimulation, all particles within $\sim 2r_{200}$ from its centre are traced back to the initial conditions and their positions on the original cubic grid are recorded. A box of size $L_{\rm sbox}$ enclosing all of these particles is then defined.

A displacement field is generated for $N_{\rm sbox} = 256^3$ particles in this new box using a two-step procedure that allows for the inclusion of fluctuations from the original periodic box. In the first step, displacements for the $N_{\rm sbox}$ particles are calculated using the *same* Fourier representation as in the original box, except for the contribution from wavelengths shorter than a characteristic scale, $d_{\rm lcut}$. Typically, $d_{\rm lcut}$ is chosen to be the shortest wavelength in the original box, $d_{\rm lcut} = 2L_{\rm box}/N_{\rm box}^{1/3} = 2 \times 32.5/128\,h^{-1}{\rm Mpc} \sim 0.5\,h^{-1}$ Mpc, which is the Nyquist wavelength of the low-resolution particle grid. We truncate the waves at a boundary that is cubical in Fourier space.

It is important to ensure that the displacements as a result of the long wavelength Fourier components are applied to the high-resolution particles in a sufficiently smooth fashion to avoid introducing significant spurious power. Computing the displacements by simple finite differencing of the potential, as is the case for the large periodic simulation box, is inadequate in this context unless an impractically large mesh is deployed. A better way is to compute the individual components of the displacement field one at time, using the appropriate Green's functions, and to interpolate the displacement components themselves, by trilinear interpolation to the individual particle positions. The use of trilinear interpolation ensures that the displacement field is continuous – which in itself is sufficient to avoid spurious non-linear features being introduced. The larger the mesh used, the more accurate is the interpolation. For the simulations reported here, a $512^3$ mesh was used and proved satisfactory.

In the second step, fluctuations are generated on scales smaller than $d_{\rm lcut}$, down to the Nyquist frequency of the high-resolution

box. The new displacement field is periodic within $L_{\rm sbox}$, and can be vector added to the large-box displacements in order to obtain final perturbed positions for all particles within the high-resolution box. Trilinear interpolation is once again used to assign the short-wave components of the displacement field to the particles. Peculiar velocities proportional to the displacements are then assigned using the Zel'dovich approximation and assuming that only growing modes are present.

Following this procedure, a realization of the displacement field of $256^3$ particles is created and stored for each halo. Finally, the high-resolution box is inserted in the large periodic box after removal of all overlapping particles. Not all particles in the small box will end up near the system of interest, so the location on the original grid of selected particles is used to identify an 'amoeba-shaped' region within the cube that is retained at full resolution. Regions exterior to the 'amoeba' are coarse-sampled using particle masses which increase with distance from the region of interest (Fig. 2). The sampling is typically performed by binning together cubes of $2^{3n}$ neighbouring particles from the initial grid (where $n$ is an integer). This allows us to concentrate numerical resources within our selected object without compromising the contribution from larger scales to the tidal field acting on the system. Because of the non-spherical nature of the collapse of dark haloes, accurate simulation of the formation of a single system incurs a significant overhead. Even after all this optimization, at most one in three particles in the amoeba region ends up within the virial radius of the system considered.

The success of our procedure may be gauged by computing the power spectrum from the displaced particle positions and comparing it with the theoretical power spectrum that we are trying to generate. Fig. 1 shows the desired theoretical power spectrum, the power spectrum measured from the parent simulation, and the power spectrum measured from a high-resolution box created in the manner outlined above. The power spectra are shown at $z = 49$. In this case, the high-resolution box is $5.08\,h^{-1}$ Mpc on a side and is sampled with $256^3$ particles, with individual masses of $6.5 \times 10^5\,h^{-1}\,M_\odot$. The power spectrum of the small box is actually determined for a cube of $4.3\,h^{-1}$ Mpc excised from the middle of the high-resolution region. The excised region would contain $216^3$ particles if it had precisely mean density. The density field is assigned to a $432^3$ mesh using a cloud-in-cell assignment scheme and periodic boundary conditions forced. Forcing periodicity does not significantly distort the power spectrum for modes that are small compared to the fundamental mode of the cube. The power spectrum is then computed from the Fourier transformed density field. The power from individual modes is binned in shells of constant cubical wavenumber ($k_{\rm cubical} = \max(|k_x|, |k_y|, |k_z|)$). Plotting the power spectrum using the cubical wavenumber highlights discrepancies more sharply than the more usual spherical binning. The good agreement between the theoretical power spectrum and that measured in our realizations gives us confidence that our simulations faithfully follow the formation of a dark matter halo in the $\Lambda$CDM cosmogony.

This paper has been typeset from a TeX/LaTeX file prepared by the author.